

Article

# Solvothermally Grown Oriented WO<sub>3</sub> Nanoflakes for the Photocatalytic Degradation of Pharmaceuticals in a Flow Reactor

Mirco Cescon<sup>1</sup> , Claudia Stevanin<sup>2</sup>, Matteo Ardit<sup>3,4</sup> , Michele Orlandi<sup>5</sup> , Annalisa Martucci<sup>4</sup> ,  
Tatiana Chenet<sup>2</sup>, Luisa Pasti<sup>2,\*</sup> , Stefano Caramori<sup>1,6,\*</sup> and Vito Cristino<sup>1</sup>

<sup>1</sup> Department of Chemical, Pharmaceutical and Agricultural Sciences, University of Ferrara, Via L. Borsari 46, 44121 Ferrara, Italy; mirco.cescon@unife.it (M.C.); vito.cristino@unife.it (V.C.)

<sup>2</sup> Department of Environmental and Prevention Sciences, University of Ferrara, Via L. Borsari 46, 44121 Ferrara, Italy; claudia.stevanin@unife.it (C.S.); tatiana.chenet@unife.it (T.C.)

<sup>3</sup> Department of Geosciences, University of Padova, Via Gradenigo 6, 35131 Padova, Italy; matteo.ardit@unipd.it

<sup>4</sup> Department of Physics and Earth Sciences, University of Ferrara, Via Saragat 1, 44121 Ferrara, Italy; annalisa.martucci@unife.it

<sup>5</sup> Department of Physics, University of Trento, Via Sommarive 14, 38123 Trento, Italy; michele.orlandi@unitn.it

<sup>6</sup> National Interuniversity Consortium of Materials Science and Technology (INSTM), University of Ferrara Research Unit, 44121 Ferrara, Italy

\* Correspondence: luisa.pasti@unife.it (L.P.); stefano.caramori@unife.it (S.C.);  
Tel.: +39-0532455346 (L.P.); +39-0532455474 (S.C.)

**Abstract:** Contamination by pharmaceuticals adversely affects the quality of natural water, causing environmental and health concerns. In this study, target drugs (oxazepam, OZ, 17- $\alpha$ -ethinylestradiol, EE2, and drospirenone, DRO), which have been extensively detected in the effluents of WWTPs over the past decades, were selected. We report here a new photoactive system, operating under visible light, capable of degrading EE2, OZ and DRO in water. The photocatalytic system comprised glass spheres coated with nanostructured, solvothermally treated WO<sub>3</sub> that improves the ease of handling of the photocatalyst and allows for the implementation of a continuous flow process. The photocatalytic system based on solvothermal WO<sub>3</sub> shows much better results in terms of photocurrent generation and photocatalyst stability with respect to state-of-the-art WO<sub>3</sub> nanoparticles. Results herein obtained demonstrate that the proposed flow system is a promising prototype for enhanced contaminant degradation exploiting advanced oxidation processes.

**Keywords:** pharmaceuticals; photocatalytic prototype system; solvothermally grown WO<sub>3</sub>; water remediation



**Citation:** Cescon, M.; Stevanin, C.; Ardit, M.; Orlandi, M.; Martucci, A.; Chenet, T.; Pasti, L.; Caramori, S.; Cristino, V. Solvothermally Grown Oriented WO<sub>3</sub> Nanoflakes for the Photocatalytic Degradation of Pharmaceuticals in a Flow Reactor. *Nanomaterials* **2024**, *14*, 860. <https://doi.org/10.3390/nano14100860>

Academic Editors: Pedro Manuel Martins and Noelia González-Ballesteros

Received: 18 April 2024  
Revised: 8 May 2024  
Accepted: 14 May 2024  
Published: 15 May 2024



**Copyright:** © 2024 by the authors. Licensee MDPI, Basel, Switzerland. This article is an open access article distributed under the terms and conditions of the Creative Commons Attribution (CC BY) license (<https://creativecommons.org/licenses/by/4.0/>).

## 1. Introduction

In recent years, a significant influx of new contaminants has adversely affected the quality of both surface and groundwater on a global scale. The increase in human life expectancy, coupled with population growth, has led to an escalation in the use of pharmaceuticals [1,2]. Consequently, this has enhanced the presence of drugs in aquatic environments, resulting in a comprehensive list that undergoes continuous updates. The growing reports of the detection of these contaminants in surface waters worldwide is a cause for concern. Their presence in the aquatic environment can induce alterations in the physiological conditions and behavior of aquatic organisms. In particular, among bioactive environmental contaminants, steroid hormones are considered of high priority due to their biological activity, widespread use, and potential to interfere in endocrine functions (e.g., reproductive dysfunction) after exposure [3,4]. Drospirenone (DRO) (Figure 1), a synthetic progestin used in oral contraceptives, is frequently combined with 17- $\alpha$ -ethinylestradiol (EE2) (Figure 1) [5]. It is one of the most prescribed synthetic progestins in numerous European countries and it is extensively used, especially in the USA. Due to their extensive

use, both molecules have been detected in wastewaters and surface waters [6]. It has been demonstrated that fish species, such as adults and embryos of zebrafish (*Danio rerio*), exposed to DRO showed alteration in the gene transcription involved in hormone homeostasis, leading to reproductive changes and significant alterations of circadian rhythm [6,7]. Similarly, in surface waters, the synthetic estrogen EE2 can be found as a ubiquitous contaminant; indeed, EE2 at environmentally relevant concentration levels presents adverse effects on fish, including decreased egg fertilization, reproduction disruption, feminization, induction of vitellogenin, and increased mortality [8]. Due to its potential adverse effect on biota and human health, a similar estrogen (17 $\beta$ -estradiol) has been listed in Japanese Drinking Water Quality Standard [9]. In fact, EE2 considered as a priority micropollutant, as suggested by the European Union, might be regulated in the Drinking Water Quality Standards of European countries in the future [8].

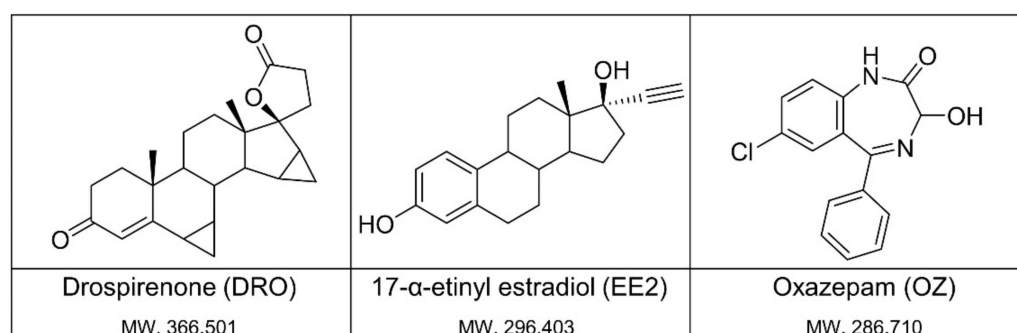


**Figure 1.** Molecular structure of drospirenone (DRO), 17- $\alpha$ -ethynylestradiol (EE2) and oxazepam (OZ). The molecules are all represented in their neutral form.

Recent research reports that municipal wastewater treatment plants (WWTPs) are the main sources of EE2 and DRO [6,8] in effluents, and consequently, in surface waters, highlighting the importance of enhancing pharmaceutical removal performance of municipal WWTPs. Concentrations of DRO and EE2 in surface waters evaluated in many countries were found up to 4.3 ng L<sup>-1</sup> and 21.5 ng L<sup>-1</sup>, respectively [9–11]. For what concerns psychoactive substances, oxazepam (OZ) (Figure 1) belongs to a family of pharmaceuticals called the benzodiazepines. In European river water, oxazepam is the benzodiazepine that is detected with the highest frequency (85%), with a maximum concentration of 61 ng L<sup>-1</sup> [12]. Close to the outlet of WWTPs, OZ concentrations can reach several hundreds of ng L<sup>-1</sup> to low ng L<sup>-1</sup> concentrations, depending on the size of the receiving river and the season [13,14]. Psychoactive substances can raise behavioral alterations that may lead to profound, nonlinear, and perhaps unpredictable ecological effects [15]. One of the main sources of the mentioned contaminants are the effluents of WWTPs; therefore, it is important to develop innovative technologies to efficiently remove those contaminants from water in order to avoid the adverse effects on water and prevent irreversible damage to the aquatic ecosystems. Nowadays, different approaches for the removal of emergent contaminants (ECs) are employed, such as the use of adsorbent materials and advanced oxidation processes (AOPs) [14]. AOPs can be used as a pre-treatment [16,17] process to improve wastewater quality and remove organic contaminants by oxidation through reactions with hydroxyl radicals (OHs) which, being a strong oxidant characterized by an oxidation potential equal to  $E^\circ = +2.1$  V vs. NHE, allows for the oxidation of a variety of organic substances, leading to their mineralization [18–20]. To reduce the energetic request for implementing redox remediation processes, photocatalytic materials show some promise.

The ability of some semiconductors to adsorb UV–vis photons for the production of highly energetic electron/hole pairs makes these materials capable of promoting thermodynamically demanding oxidation reactions. In particular, some metal oxide semiconductors like TiO<sub>2</sub>, ZnO and WO<sub>3</sub> display such a deep valence band, whose edge bears the prevailing contributions by  $\pi$  orbitals of the oxygen atoms, that holes therein generated are able to pro-

duce hydroxyl radicals following mono-electronic water oxidation. The wide band gap of many metal oxide semiconductors can limit the portion of absorbed solar light; for example, TiO<sub>2</sub> and ZnO have a sizable photochemical activity only upon UV excitation. A good compromise between the need for generating powerfully oxidizing holes and the harvesting of solar light is incorporated in WO<sub>3</sub>, being able to absorb photons up to 460 nm (band gap of ca. 2.7 eV). The ability of WO<sub>3</sub> to generate ·OH through water oxidation under visible illumination has been previously reported [21]. A variety of techniques can be used to synthesize efficient WO<sub>3</sub> structures aimed at increasing the photon-to-electron conversion by emphasizing the surface (contact) area of the photocatalyst, thus reducing electron/hole recombinative losses; pulsed laser deposition [22], electrochemical anodization [23–26], sputtering [27], evaporation [28], sol-gel [29–31], electrophoresis [32], hydrothermal and solvothermal [33–35] are some of the techniques described in the scientific literature.

Besides achieving a high photoconversion efficiency, the choice of the preparative technique to afford a practical photocatalytic system for water decontamination should consider other aspects as well. The low cost and abundance of reagents and of preparative equipment, the potential for scaling-up the synthesis, the possibility to support the catalytic material to facilitate the handling of the photocatalyst, and the ability to implement a flow rather than a “batch” process are some of the issues to consider for the successful implementation of a photocatalytic route-to-water decontamination. Large-scale wastewater treatment plants require a continuous operation unit able to process large volumes of liquid, which is generally difficult and economically disadvantageous with batch reactors. For these reasons, in this study, we tested the capabilities of solvothermal WO<sub>3</sub> (WO<sub>3</sub>/st), prepared using a scalable solvothermal route and stabilized with a TiO<sub>x</sub> adhesion layer, in the oxidative degradation of selected emerging chemical contaminants using both a batch method and a flow system based on a reactor packed with WO<sub>3</sub>/st-modified glass beads.

## 2. Materials and Methods

### 2.1. Chemicals for Analytical and Photochemical Experiments

Drospirenone (DRO) was purchased from European Pharmacopoeia Reference Standard (purity 100%), 17- $\alpha$ -ethynylestradiol (EE2) from Dr. Ehrenstorfer GmbH (Augsburg, Germany) (purity > 96.3%), while oxazepam (OZ) was obtained from F.I.S. Fabbrica Italiana Sintetici S.p.a. (Vicenza, Italy) (purity 100%); Na<sub>2</sub>SO<sub>4</sub> from VWR International S.r.l. (Milan, Italy) (purity > 99%), acetonitrile (ACN) and phosphoric acid were purchased from Merck KGaA (Darmstadt, Germany) (HPLC grade, purity > 99%), H<sub>2</sub>WO<sub>4</sub> and oxalic acid dihydrate were purchased from Alfa Aesar (Haverhill, MA, USA) (purity 99.5–102.5%), hydrogen peroxide (purity 35%) and  $\alpha$ -phenyl *N*-tert-butyl nitrene were purchased from Merck KGaA, lithium perchlorate was purchased from Acros Organics (Geel, Belgium) (purity 99%), hydrochloric acid was purchased from Carlo Erba Reagents S.r.l. (Milan, Italy) (37%). All the solutions were prepared using ultrapure waters (Milli-Q<sup>®</sup> systems, Merck KGaA, Darmstadt, Germany).

### 2.2. Synthesis of WO<sub>3</sub>/st Films and Powder by Solvothermal Method

WO<sub>3</sub>/st nanocrystalline film was grown either on commercial glass spheres (GS), with a diameter of 4 mm, microscope glass slides (MGSs) or a fluorinated tin oxide glass (FTO glass, TEC 7  $\Omega$  supported on soda lime glass; Pilkington, Lathom, UK) substrate. All substrates were cleaned by ultrasonication for 10 min in 2-propanol prior to use. The preparation of the photocatalytic substrates was accomplished according to three sequential steps.

Step 1: Before the deposition of WO<sub>3</sub>/st, the formation of a TiO<sub>x</sub> nanometric adhesion layer (<5 nm) was accomplished by the room temperature hydrolysis of TiCl<sub>4</sub> on the oxide supports (GS, MGS, FTO). Specifically, the soaking of the supporting surfaces in 0.4 M TiCl<sub>4</sub> was carried out for 12 h for GS and MGS and 6 h in the case of FTO. After abundant rinsing of the glass substrates with deionized water, firing for 30 min at 450 °C in air afforded the desired TiO<sub>x</sub> adhesion layer which, as we will demonstrate, does not block the

collection of the photocarriers generated within  $\text{WO}_3$  upon band gap excitation (Figure S1).  $\text{WO}_3$  substrates obtained on top of the  $\text{TiO}_x$  adhesion layer are named  $\text{WO}_3$ -Ti-substrate (i.e.,  $\text{WO}_3$ -Ti-FTO) and, unless otherwise indicated, all photocatalytic materials herein investigated are of the type  $\text{WO}_3$ -Ti.

Step 2: In the case of planar substrates, prior to solvothermal deposition, a  $\text{WO}_3$  seed layer with a thickness on the order of a few nanometers (typically 10–30 nm) was obtained by spin coating (9 s at 1000 rpm, 20 s at 2000 rpm); the precursor used for this process can be either 0.5 M peroxotungstic acid (PTA) or a colloidal precursor based on previously reported methods [29]. Such a precursor layer is converted into  $\text{WO}_3$  by firing at 550 °C in air. The best results were obtained with the peroxotungstic acid precursor. While the presence of the  $\text{WO}_3$  seed layer emphasizes the surface coverage and density of the photoactive film, its absence does not preclude the subsequent hydrothermal growth of the porous  $\text{WO}_3$ /st layer.

Step 3: The solvothermal (st) deposition of  $\text{WO}_3$  on top of the glass substrates was treated according to steps 1 and 2 (optional), followed a procedure described by Grimes et al. [35]. In a typical preparation of the synthesis of a dense  $\text{WO}_3$  photocatalytic layer based on oriented lamellar arrays or nanoflakes, the precursor solution was prepared by dissolving 1.25 g of  $\text{H}_2\text{WO}_4$  in 10 mL of ultrapure water and 10 mL of 35% *w/w*  $\text{H}_2\text{O}_2$  while heating and stirring bain-marie at 95 °C. In total, 18 mL of this  $\text{H}_2\text{WO}_4$  solution (0.25 M), plus 1.2 g of oxalic acid and 3 mL of HCl (6 M), were mixed into 60 mL of acetonitrile and 15 mL of ultrapure water. Glass substrates, either flat slides or beads, were immersed in such a solution and heated at 180 °C in a Teflon-lined steel autoclave for a duration variable from 1 h to 30 min for glass spheres and 2 h for FTO. Besides the coated materials,  $\text{WO}_3$ /st powder was also recovered from the bottom of the Teflon reactor, washed with distilled water, and dried in an oven at 60 °C for a few hours. All  $\text{WO}_3$ /st-coated substrates were fired at 500 °C in air for 2 h to obtain the sintering and crystallization of  $\text{WO}_3$ /st. Similar thermal treatment was used with the material in the form of a powder.

### 2.3. Structural Characterization Techniques

#### 2.3.1. X-ray Powder Diffraction

Data from samples grown on flat surfaces were collected at room-temperature conditions (RT). Data collection was performed on a diffractometer (D8 Advance Davinci, Bruker Corporation, Billerica, MA, USA), working in Bragg–Brentano geometry, and equipped with a Cu-anode X-ray tube, Ni-filter to suppress the Cu  $\text{K}\beta$  component, and a LynxEye XE silicon strip detector (angular range of the detector window size =  $2.585^\circ 2\theta$ ) set to discriminate Cu  $\text{K}\alpha_{1,2}$  radiation.

Samples were loaded in a poly-(methyl methacrylate) specimen holder characterized by a cavity with adjustable depth to properly fit the microscope slide thickness, and scanned in a continuous mode from  $5$  to  $90^\circ 2\theta$ , with step size of  $0.02^\circ 2\theta$  and a counting time of 3 s per step. A knife perpendicular to the sample holder placed at a sub-millimetric distance from the sample was used to reduce the air-induced scattering.

Rietveld refinement. Collected XRPD patterns were modelled by means of the fundamental-parameter Rietveld approach (TOPAS v.5.0, Bruker Corporation, Billerica, MA, USA). Identified phases were modelled by carrying out a multiphase refinement in which only the scale factors and unit-cell parameters were varied. Instrumental parameters (e.g., goniometer radius, slit sizes, geometrical parameters of the X-ray tube, etc.) were used to calculate the instrumental contribution to the peak profiles, and specimen-related crystallite size information for each phase was extracted from the observed profile. An instrumental zero-error was fixed at the value, determined using the Si Standard Reference Material (640e, National Institute of Standards and Technology, Gaithersburg, MD, USA) standard, and the refinement included a specimen displacement correction and a Chebyshev polynomial to model the background.

### 2.3.2. Scanning Electron Microscopy

The morphological characterization of WO<sub>3</sub> films, on FTO substrate, was performed using a scanning electron microscopy (SEM, JSM-7001F FEG-SEM, JOEL Ltd., Tokyo, Japan) equipped with an energy-dispersive X-ray spectroscopy detector (EDXs, Oxford INCE PentaFETx3, Oxford Instruments Plc., Abingdon, UK). A 90° stub was used to define the thickness and the different layers of the electrode.

### 2.3.3. Photoelectrochemical Characterization

Photoelectrochemical studies were carried out by exploiting the WO<sub>3</sub> films grown on FTO. The typical photoelectrochemical cell was composed of an FTO/WO<sub>3</sub> working electrode, a platinum wire counter electrode, and a saturated calomel electrode (SCE) reference electrode. Current/potential (J/V) curves were collected under simulated solar light using a solar simulator (ABET Technologies Inc., Milford, CT, USA) equipped with a AM1.5G filter, with a radiant power of 100 mW/cm<sup>2</sup> and a 380 nm UV cut-off filter. The comparative measurements of WO<sub>3</sub>/st and WO<sub>3</sub>/coll were performed in an aqueous solution containing 0.7 M Na<sub>2</sub>SO<sub>4</sub> as electrolyte, in a potential range between −0.3 V to 1.5 V versus SCE with a scan rate of 0.02 V/s. To reveal the effect of hole scavenging at the WO<sub>3</sub>/st interface by the selected contaminants, J/Vs were performed in an acetonitrile (ACN) solution, using 0.1 M LiClO<sub>4</sub> as electrolyte, to bypass the low solubility of our target molecules in an aqueous solution. In this case, J/V curves were performed in a potential range between 0.1 and 1.7 V versus SCE with a scan rate of 0.02 V/s. J/V curves under pulsed illumination were obtained with an automatic shutter (SHB1T, Thorlabs, Newton, NJ, USA) at 0.3 Hz.

Cyclic voltammetry was performed in an aqueous solution containing 0.1 M LiClO<sub>4</sub> and 0.01 M K<sub>4</sub>FeCN<sub>6</sub>.

The incident photon-to-current conversion efficiency (IPCE) describes the photocurrent collected per incident photon flux as a function of the illumination wavelength. IPCE data, sampled at 10 nm intervals in the 310–500 nm range, were acquired in 0.7 M Na<sub>2</sub>SO<sub>4</sub> using the same three-electrode configuration described above. Limiting photocurrents were collected at 1 V and 1.5 V for WO<sub>3</sub>/st and WO<sub>3</sub>/coll, respectively. Here, WO<sub>3</sub>/coll denotes a mesoporous WO<sub>3</sub> electrode composed of nanoparticles (Figure S2), described in various previous publications [21,23].

The experimental setup used for photo-action spectra consisted of a monochromator (Applied Photophysics Ltd., Leatherhead, UK) equipped with a 175W Xe lamp (Luxtel-Sunoptic Technologies Inc., Jacksonville, FL, USA), various optical elements, a digital multimeter (34401A 6-1/2, Agilent Technologies Inc., Santa Clara, CA, USA), a potentiostat (552, AMEL S.r.l., Milan, Italy), and a calibrated silicon photodiode (OSD 7Q, Centronic Ltd., New Addington, UK).

Absorbed photon-to-current efficiency (APCE) spectra were computed, normalizing the IPCE value for the absorbed photons, after subtracting the reflected or transmitted photons.

$$A(\lambda) = 100 - R\%(\lambda) - T\%(\lambda) \quad (1)$$

APCE is thus dependent on the quantum efficiencies of charge transport and interfacial separation defined as follows:

$$APCE(\lambda) = IPCE(\lambda)/a(\lambda) = \eta_{\text{transport}} \eta_{\text{interface}} \quad (2)$$

considering that the efficiency of charge generation ( $\eta_e/h$ ) is unitary in a semiconductor upon band gap excitation.

### 2.3.4. EPR

EPR spin-trapping experiments were carried out with a Bruker MRD spectrometer equipped with a TE 201 resonator (microwave frequency of 9.4 GHz). The samples were suspensions of WO<sub>3</sub> used for film fabrication in aqueous solutions containing  $\alpha$ -phenyl

*N*-tert-butyl nitron (pbn,  $5 \times 10^{-2}$  M) as a spin trap. The samples were put into a flat quartz cell and directly irradiated ( $\lambda > 400$  nm) in the EPR cavity with a medium-pressure mercury lamp. No EPR signals were obtained in the dark and during the irradiation of the solution in the absence of  $\text{WO}_3$ .

#### 2.4. Photochemical Degradation Experiments

**Batch experiments.** Photodegradation tests were performed using the batch method, where a solution with a known concentration of a contaminant is placed in contact with a known quantity of  $\text{WO}_3/\text{st}$  powder (70 mg) as a photocatalytic dispersion. The photodegradation tests were carried out in 20 mL flasks under constant stirring for 300 min at room temperature (Figure S3). The solutions were irradiated using a solar simulator (ABET Technologies Inc., Milford, CT, USA, equipped with a AM1.5G filter, with a radiant power of  $100 \text{ mW/cm}^2$  and 380 nm UV cut-off filter), a device that provides illumination approximating natural sunlight. For each solution containing  $4 \mu\text{g/mL}$  of a drug (EE2, DRO and OZ) in a  $0.7 \text{ mM Na}_2\text{SO}_4$  aqueous solution at  $\text{pH} = 6 \pm 0.30$ , the following four tests were carried out under different conditions: (i) a dark test to evaluate the adsorption of contaminants at the glassware walls; (ii) a dark test, in the presence of powdered  $\text{WO}_3/\text{st}$ , to evaluate the adsorption of drugs at the surface of the solid photocatalyst; (iii) an irradiation test without  $\text{WO}_3/\text{st}$  to verify the direct photochemical degradation of each contaminant; and (iv) irradiation cycles in the presence of the photocatalyst to reveal the photodegradation deriving from the  $\text{WO}_3/\text{st}$  activity. At the end of each experiment, the separation of the supernatant was achieved by centrifugation, and the supernatants containing OZ and DRO were analyzed by HPLC-DAD (see Section 2.6), whereas EE2 solutions were analyzed by HPLC-FLD (see Section 2.7).

**Flow system experiments.** Moving from batch experiments to the flow system, a 10-fold scale-up in terms of volume was achieved, reaching a total treated water volume of 200 mL. The apparatus was composed of a glass flask, containing the polluted solution, a magnetic stirrer and a glass column containing glass spheres (GSs) coated with  $\text{WO}_3/\text{st}$  ( $\text{WO}_3/\text{st-GS}$ ) (Figure 2). The column was completely enveloped by an LED stripe ( $395 < \lambda < 400$  nm, Figure 2e) to obtain a uniform illumination of the whole packed tube and increase the probability of photon absorption by the photocatalyst along the whole tube length. The emission range of LEDs was selected in order to maximize the efficiency of photoconversion, peaking, in the  $\text{WO}_3$  photocatalyst, at the edge of the visible spectrum (Figure 2d). The average irradiance generated by the LED strip was  $49 \text{ mW/cm}^2$ .

The water flow was controlled by a peristaltic pump to  $7 \text{ mL/min}$ . Typical illumination cycles of 480 min under electrolyte recirculation conditions at room temperature were carried out by using an aqueous test solution containing  $4 \mu\text{g/mL}$  of the selected drugs in  $0.7 \text{ mM Na}_2\text{SO}_4$  at  $\text{pH} = 6.00 \pm 0.30$  (Five Easy F20, Mettler-Toledo International Inc., Greifensee, Switzerland). Similar to batch tests, various control experiments under different conditions were performed. The flow system connection tubes were selected in consideration of a low surface affinity towards the various contaminants in order to minimize drug losses by adsorption. To keep a tight packing of  $\text{WO}_3/\text{st-GS}$  in the column, PE screw caps and PP frits were placed at the inlet and outlet of the column. The electrolyte was sampled during the degradation experiments to evaluate the kinetics of the process by verifying the concentration of drugs in the solution and the formation of by-products.

#### 2.5. Kinetic Models

Chemical kinetics are a part of science with the theoretical purpose of determining the mechanism of a reaction. Among the different models to study and understand the mechanism, the experimental data were well described by the first order kinetic model (3). First order reactions are those reactions whose rate depends on the concentration of a single reactant raised to an exponent of 1. The mathematical equation is as follows:

$$\ln[C]/[C_0] = -kt \quad (3)$$

where,  $[C]$  is the reagent concentration at time  $t$ ,  $[C_0]$  is the initial concentration of the reagent,  $k$  is the kinetic constant and  $t$  is the time of reaction [36,37].

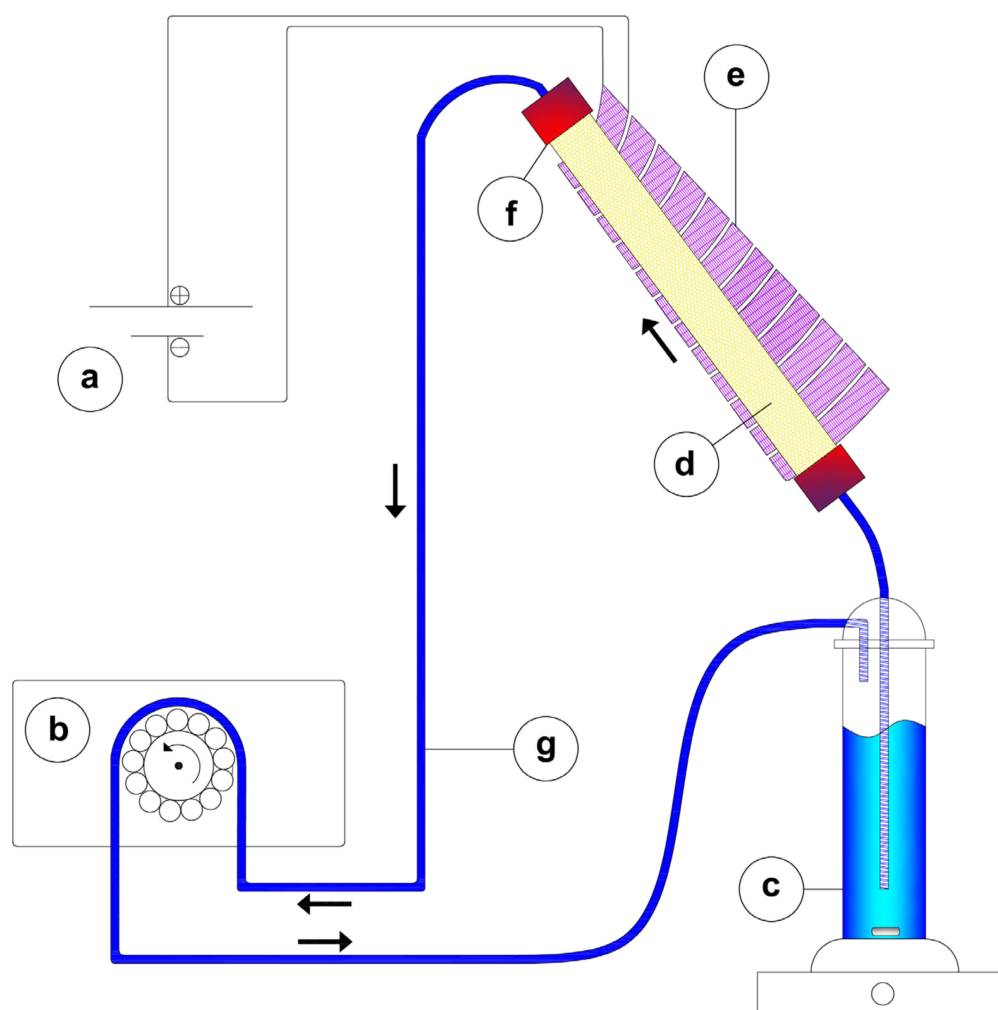


**Figure 2.** Flow system: (a) 24 V direct-current generator (DC); (b) peristaltic tube pump with two sprung rollers; flow rate set at  $7 \text{ mL min}^{-1}$ ; (c) mixing system on magnetic stirrer; (d)  $\text{Ø}3 \text{ mm}$  glass spheres,  $\text{WO}_3$ -coated ( $\text{WO}_3/\text{st-GS}$ ), confined in a glass column with internal  $\text{Ø}19 \text{ mm}$  and outer  $\text{Ø}22 \text{ mm}$ ; (e) 24 V LED source,  $\lambda = 395\text{--}400 \text{ nm}$ , completely enveloped column; (f) PE screw cap to fix a frit in PP with 2 mm grill in order to lock spheres; and (g) tubing, internal  $\text{Ø}4 \text{ mm}$  and outer  $\text{Ø}7 \text{ mm}$ .

### 2.6. HPLC-DAD Analysis

OZ and DRO removal was evaluated by HPLC-DAD analysis. The apparatus was composed of two pumps (515 HPLC pump, Waters Corp., Milford, MA, USA), Rheodyne injectors (IDEX Corporation, Northbrook, IL, USA) with  $20 \mu\text{m}$  loop and a photodiode array detector (996 DAD, Waters corp., Milford, MA, USA). The column selected was C18 100A  $150 \times 4.6 \text{ mm}$  with a particle size of  $5 \mu\text{m}$  (Kinetex SuXB, Phenomenex, Torrance, CA, USA). The mobile phase was a mixture of acetonitrile (ACN) and ultrapure  $\text{H}_2\text{O}$ , and the analyses were performed under isocratic conditions. The flow rate was  $1 \text{ mL/min}$ , and the injection volume was  $20 \mu\text{L}$ . For the OZ molecule, the mobile phase mixture was 40% ACN and 60%  $\text{H}_2\text{O}$ , while for the DRO molecule, the eluent was 50% ACN and 50%  $\text{H}_2\text{O}$ . OZ and DRO were detected at 227 nm and 265 nm, respectively.

### 2.7. HPLC-FLD Analysis

EE2 analysis was performed using an HPLC (1290 Infinity, Agilent Technologies Inc., Santa Clara, CA, USA) equipped with a binary pump, autosampler, thermostatic column compartment, and fluorescence detector (FLD 1290 Infinity II, Agilent Technologies Inc., Santa Clara, CA, USA). The selected column was C18 100A 150 × 4.6 mm with a particle size of 5 μm (Kinetex SuXB, Phenomenex, Torrance, CA, USA). The column compartment temperature was set to 25 °C. The eluent mixture consisted of 70% ACN and 30% ultrapure water, and the analysis was performed under isocratic conditions; the flow rate was 1 mL/min, and the injection volume was 20 μL. The detection conditions were set to an excitation wavelength of 280 nm and an emission wavelength of 310 nm.

### 2.8. HPLC-MS Analysis

HPLC/MS analyses were carried out by means of Surveyor micro-HPLC hyphenated to a linear trap quadrupole mass spectrometer (LTQ XL, Thermo Fisher Scientific Inc., Waltham, MA, USA). The HPLC was composed of a solvent delivery system, a quaternary pump and an autosampler. The LTQ system was equipped with an electrospray ionization (ESI) ion source. The mobile phase was obtained by mixing ACN/0.1% *v/v* formic acid with ultrapure water/0.1% *v/v* formic acid according to the following gradient program: 0 min 10% ACN, 0–10 min 10–90% ACN, and 10–12 min 90% ACN. Then, the column was reconditioned at 10% ACN until reaching 15 min of elution time. The flow rate was 150 μL/min. The column was C-18 100 mm × 2.1 mm × 2.1 μm (Supelco, Bellefonte, PA, USA). The injection volume was 2 μL for all standards and samples. MS experimental conditions were as follows: spray voltage 5 kV, capillary temperature 275 °C, capillary voltage 28 V and tube lens 50 V for positive ESI conditions (OZ and DRO); spray voltage 5 kV, capillary temperature 275 °C, capillary voltage −50 V and tube lens −137 V for negative ESI conditions (EE2).

## 3. Results and Discussion

### 3.1. Morphological and Structural Properties of Nanostructured WO<sub>3</sub>

The geometrical constraints of the GS make it impossible to perform a reliable structural and morphological characterization of WO<sub>3</sub> nanostructures decorating these curved supports. Nevertheless, the structural properties of WO<sub>3</sub> films obtained on flat surfaces, consisting of both FTO and simple glass, are considered representative of the general properties of the WO<sub>3</sub> coating on the glass beads. In addition, the use of conductive FTO allows us to quantify, via photoelectrochemical measurements, the performance of these WO<sub>3</sub> substrates in generating reactive charge carriers when excited with suitable optical frequencies.

#### 3.1.1. Electron Microscopy

The presence of the TiO<sub>x</sub> adhesion layer is not clearly discernible on the FTO surface, indicating that its thickness is below the instrumental detection limit (5 nm in cross section mode on this type of surface) of our SEM. At such low thickness, the crystalline and band structure of TiO<sub>x</sub> is probably unable to fully develop, resulting in a defective layer which allows electron percolation to the TCO collector to occur, as shown by cyclic voltammetry with a fast Fe (II)/III redox probe (Figure S1). Instead, the compact WO<sub>3</sub> seed layer can be clearly seen from Figure 3. The seed layer produced with the PTA precursor conformally covers the FTO substrate, which has an overall rough and irregular appearance due to the presence of large FTO crystals (hundreds of nanometers in size). The seed layer displays a thickness of about 30–40 nm, as shown in Figure 3b, and is quite homogeneous, despite the presence of cracks, in particular in the valleys between adjacent FTO crystallites, wherein the liquid precursor tends to accumulate, giving rise to a locally thicker WO<sub>3</sub> film which fractures upon thermal sintering.

The effect of the TiO<sub>x</sub> adhesion layer is macroscopically evident from the mechanical properties of the photoactive films at the end of the solvothermal growth and annealing

(Figure S4a,b). In the  $\text{WO}_3/\text{st-FTO}$  ( $\text{WO}_3/\text{st}$  = solvothermal  $\text{WO}_3$ ) samples (that is, steps 2 and 3 without the  $\text{TiO}_x$  adhesion layer), uncoated islands appear as a result of the thick  $\text{WO}_3$  film detaching from the TCO surface. Moderate magnification optical microscopy shows that the  $\text{WO}_3$  film crinkles and peels off the surface because of poor adhesion, or thermal stresses during the annealing, leaving exposed FTO underneath. Actually, the  $\text{WO}_3$ -FTO shown in Figure S4b is one of the few samples where the solvothermal  $\text{WO}_3$  layer did not detach completely from the FTO ohmic contact upon rinsing and annealing. When the same procedure is carried out after the  $\text{Ti(IV)}$  treatment (step 1), affording the sample  $\text{WO}_3/\text{st-Ti-FTO}$ , one obtains an electrode which remains solidly and uniformly coated after the rinsing/annealing cycle. The hydrophilic  $\text{TiO}_x$  layer considerably stabilizes the  $\text{WO}_3$  adhesion to the electrode, being characterized by the presence of a higher-than-FTO density of surface OH groups. Thus, multiple oxo bridges with  $\text{WO}_3$  could be formed, guaranteeing a robust anchor to the FTO of the latter.

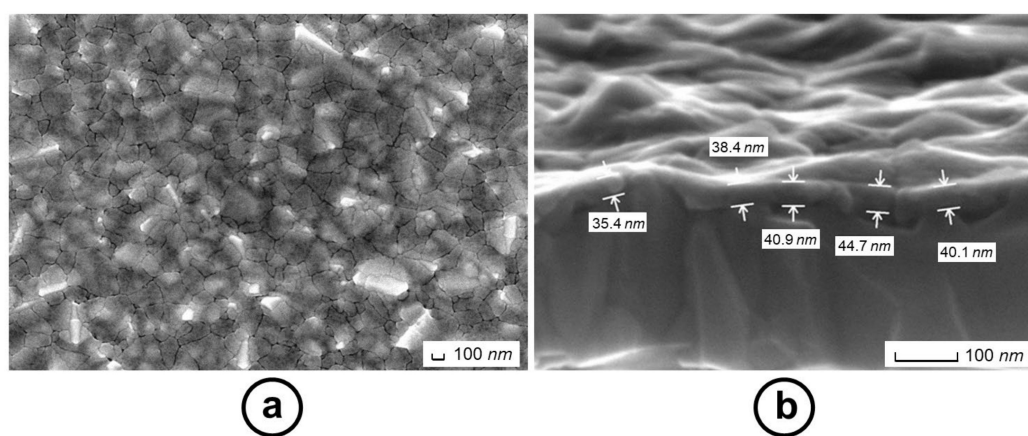


**Figure 3.** Morphology of the  $\text{TiO}_x$ -treated  $\text{WO}_3$  seed layer on FTO support imaged from the top (a) and from the side (b), showing the thickness of the deposit.

The typical surface of a  $\text{WO}_3/\text{st-Ti-FTO}$  electrode is characterized by a dense coverage of  $\text{WO}_3$  leaves and lamellae, roughly vertically aligned with respect to the surface, and arranged in somewhat organized superstructures which may resemble flowers or flakes. These leaves are relatively thin (<100 nm) (Figure 4b) compared to their length and width, which extend for several microns (Figure 4a) and could, thus, be essentially considered 2D structures. The inspection of the cross section of the electrode reveals that these lamellae extend considerably in length, taking up most of the film thickness (about 8  $\mu\text{m}$ ) and confirm their close packing and roughly vertical alignment with respect to the FTO surface. A closer inspection of the cross section reveals a disordered layer, composed mostly of nanoparticles, with the overall thickness of few 100 s of nanometer between the roots of the leaves and the seed layer. This rubble-like layer could be formed either by the partial collapse of the lamellae, or by the precipitation of  $\text{WO}_3$  during the initial stage of the solvothermal growth before thermal equilibrium is reached. Nevertheless, it is clear that either in electrodes or decorated glass supports illuminated from the top (electrolyte side), photon absorption will occur mostly within the 2D structures, which will be the primary actors in the charge transfer dynamics involving  $\text{WO}_3/\text{st}$ . In the absence of the  $\text{TiO}_x$  adhesion layer, the same lamellar morphology of the  $\text{WO}_3$  layer of Figure 4 is observed (Figure S5), although a nearly complete detachment of the  $\text{WO}_3$  film from the FTO ohmic support is observed. EDS analysis confirms the expected stoichiometry of  $\text{WO}_3$ , with tungsten and oxygen as the only significant elements in the elemental composition of the nanostructured film, appearing in a 1:3 molar ratio (Figure S6).

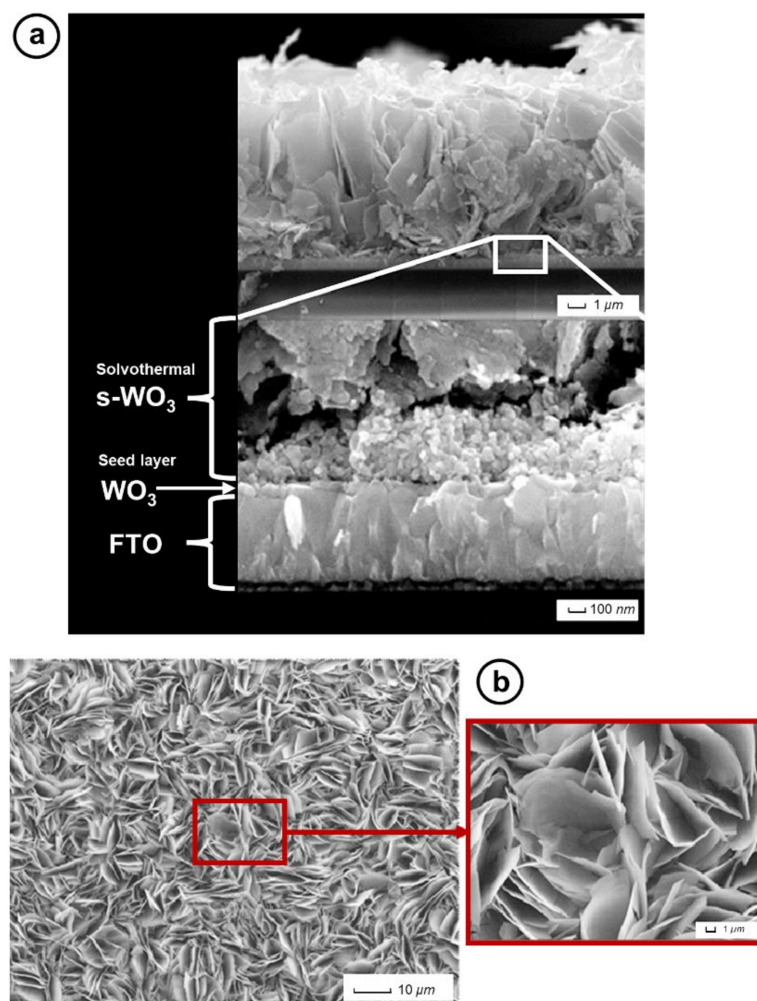


**Figure 4.** SEM imaging of  $\text{WO}_3$ - $\text{TiO}_x$ -FTO electrode in cross sectional (a) and top views (b). The magnification of the top view allows us to appreciate the thickness of the  $\text{WO}_3$ /st leaves, of less than 100 nm, compared to their length and width of several microns.

### 3.1.2. X-ray Diffraction

X-ray diffraction (XRD) data confirmed that  $\text{WO}_3$ /st on the Ti-FTO substrate was composed by high-quality monoclinic  $\text{WO}_3$ , with a P 21/n space group, formed during high-temperature annealing with cell parameters of  $a = 7.320 \text{ \AA}$ ,  $b = 7.518 \text{ \AA}$ ,  $c = 7.670 \text{ \AA}$  ( $V(\text{\AA}^3) = 422.1$ ),  $\beta = 90.4^\circ$  ( $\text{WO}_3$  database code ICSD 80056) and was marginally different from the data collected on other types of standard  $\text{WO}_3$  electrodes produced in our laboratory [37] (our colloidal standard ( $\text{WO}_3$ /coll) affords  $a = 7.303 \text{ \AA}$ ,  $b = 7.536 \text{ \AA}$ ,  $c = 7.686 \text{ \AA}$  ( $V(\text{\AA}^3) = 422.9$ ),  $\beta = 90.4^\circ$  ( $\text{WO}_3$  database code ICSD 80056), and consistent with the results reported by Grimes [35] in his paper. This confirms that the  $\text{TiO}_x$  adhesion layer does not interfere with the subsequent solvothermal growth. Crystallite size is much smaller than the size of a whole lamella, being only 25.09 nm. Thus, every leaf is formed by several nanometer-sized  $\text{WO}_3$  crystallites.

The diffraction peak at  $2\theta$  of  $23.2^\circ$ ,  $23.6^\circ$  and  $24.4^\circ$  corresponds to the (002), (020) and (200) facets (see Figure 5). The two samples show different preferentially exposed facets which are (200) for  $\text{WO}_3$ /coll and (002) for  $\text{WO}_3$ /st. A possible mechanism for solvothermal growth that explains the preferential (002) facet exposure in  $\text{WO}_3$ /st is proposed by Gong et al. [33], who state that, during the solvothermal reaction, the  $\text{Cl}^-$  functions as a kind of capping ion analogous to what was reported for  $\text{F}^-$  [38–40]. Since the (002) facets have a larger surface energy than (020) and (200) ((002) ( $1.56 \text{ Jm}^{-2}$ ) > (020) ( $1.54 \text{ Jm}^{-2}$ ) > (200) ( $1.43 \text{ Jm}^{-2}$ )),  $\text{Cl}^-$  is preferably adsorbed on the (002) facets. This adsorption weakens the

surface affinity for the precursor to this orientation, thus inhibiting the crystal growth rate along the perpendicular to these planes, resulting in the increased exposure of the (002) facets. It is well known that the reactivity of a photocatalyst is influenced by its surface atomic and electronic structure [40], so the preferential exposure of (002) instead of (200) family of planes could strongly influence the photocatalytic performance of these  $\text{WO}_3$  structures. Indeed, as reported by Gong et al. [33], the preferential exposure of (002) facets was found to improve the photoelectrochemical performance of  $\text{WO}_3$  photoanodes. According to Wang et al. [34], the preferential exposure of the highly active (001) facets that belong to the same {001} family of planes as (002) facets endows  $\text{WO}_3$  nanocrystals with significantly enhanced photocatalytic activity, which can be attributed to the stabilization of reactive oxygen species and the reduced recombination of photogenerated electrons and holes at these interfaces.

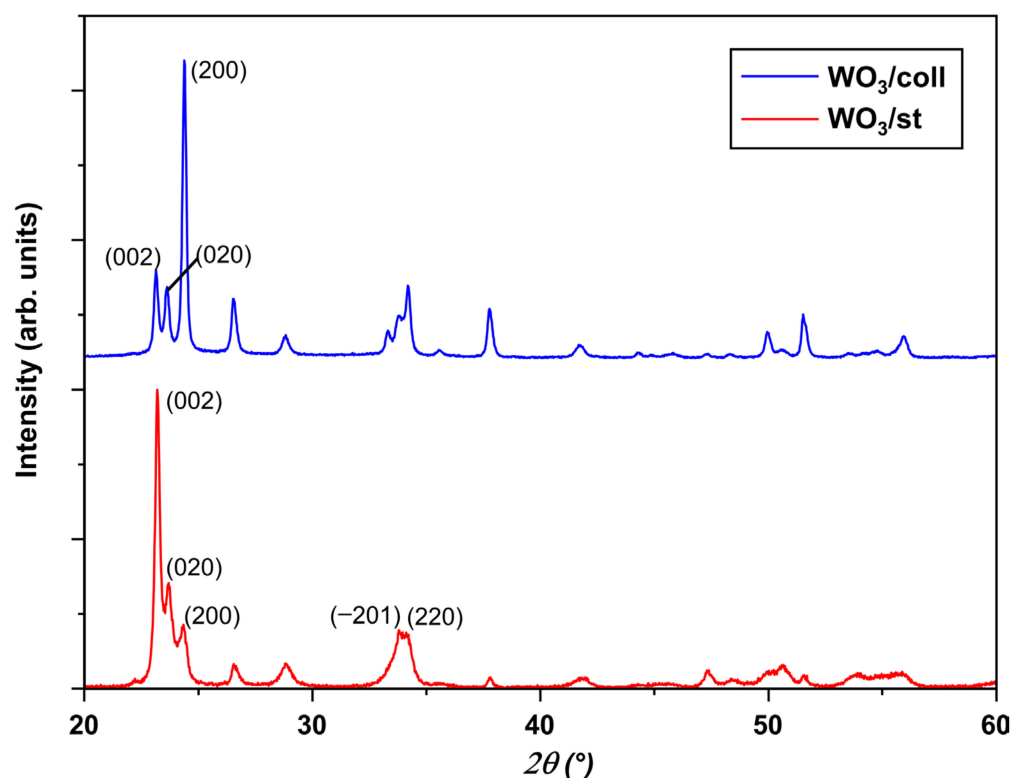


**Figure 5.** XRD patterns recorded on FTO substrate compared to the  $\text{WO}_3/\text{coll}$  standard of known art produced in our laboratory.

As concerns the  $\text{WO}_3/\text{st-Ti}$  grown on simple glass slides, a comparison of the collected X-ray diffraction patterns at RT is reported in Figure 5.

A qualitative phase analysis of the collected patterns was performed by means of the AXS EVA software (v.6.0.0.7) (Bruker Corporation, Billerica, MA, USA). Both samples were biphasic and composed of tungsten oxide  $\text{WO}_3$  in two polymorph modifications, namely monoclinic (s.g.  $P2_1/n$ ), which is largely prevalent (>95%) and hexagonal (s.g.  $P6_3/mcm$ ) (<4%). The hexagonal phase was observed previously in materials obtained through other types of hydrothermal processes, and was found to be active in oxygen evolution processes as well [41]. The presence of hexagonal/monoclinic junctions was considered beneficial for improved charge separation by some authors [42]. Prolonged exposure of  $\text{WO}_3/\text{st}$  to pH 7 water ( $\text{WO}_3$ -washed) does not change the compositional profile substantially, indicating that both phases persist on the surface of glass supports during the employment of the photocatalyst in neutral aqueous media. The Rietveld refinement plots for both samples are shown in Figures S7 and S8. Quantitative phase analysis and unit-cell parameters, as well as the crystallite size of the main phases, are summarized in Table 1.

**Table 1.** Quantitative phase analysis and unit-cell parameters, as well as the crystallite size of the main phases, for the investigated samples. The R-weighted pattern refinement agreement factor was  $R_{wp} = 0.030$  and  $0.032$  for the sample  $WO_3/st$  and  $WO_3/st$ -washed, respectively.

		Unit-Cell Parameters and Crystallite Size							
	Phase	QPA <sup>1</sup> Wt%	Space Group	a (Å)	b (Å)	c (Å)	$\beta$ (°)	V (Å <sup>3</sup> )	Crystallite Size (nm)
$WO_3$	$WO_3$ (monoclinic)	96.0 (3)	$P2_1/n$	7.3055 (8)	7.5256 (9)	7.6761 (10)	90.43 (1)	422.01 (9)	23 (1)
	$WO_3$ (hexagonal)	4.0 (3)	$P6_3/mcm$	7.354 (2)	–	7.397 (6)	–	346.5 (4)	–
$WO_3$ washed	$WO_3$ (monoclinic)	99.0 (2)	$P2_1/n$	7.3106 (8)	7.5271 (9)	7.6813 (10)	89.97 (1)	422.69 (9)	21 (1)
	$WO_3$ (hexagonal)	1.0 (2)	$P6_3/mcm$	–	–	–	–	–	–

<sup>1</sup> Quantitative Phase Analysis.

The result of the XRD investigation allows us to conclude that the nature of the support (either simple glass or TCO) does not affect the crystalline nature of  $WO_3/st$  by a large margin. Coherent scattering domains are also similar (ca. 20 nm) with either  $SnO_2:F$  or borosilicate glass supports, with different surface chemistry. This is probably due to the fact that both surfaces are modified, to stabilize the adhesion of  $WO_3/st$ , with the same adhesion ( $TiO_x$ ) and seed ( $WO_3$ ) layers. A largely prevalent monoclinic phase is found with both substrates, which is expected to play a major role in the photoinduced processes activated upon the optical excitation of the semiconductor. Furthermore, the solvothermal coating method is surprisingly easy to extend to the functionalization of a variety of substrates of shapes other than planar (i.e., irregular porous supports, glass beads) (Figure S9).

### 3.2. Photoelectrochemical Properties

Evaluating the photoelectrochemical response of  $WO_3/st$  (Figures S10 and S11) will allow us to judge the ability of these  $WO_3$  films to achieve efficient electron/hole separation, which is the primary goal and crucial for any solar energy conversion device, irrespective of its intended use in either solar fuel generation or environmental remediation processes. In addition, the information gained from photoelectrochemical experiments can be extended to the open circuit (i.e., photocatalytic) case where the efficiency figures are more elusive to obtain without ambiguity. The primary efficiency figure for this type of photoelectrochemical application is the magnitude of the current density, which is dependent on the rate of hole injection into the electrolyte, yielding OH radicals as the consequence of water oxidation. The generation of  $\cdot OH$  radicals in  $WO_3$  aqueous suspensions under visible light illumination ( $\lambda > 420$  nm) was confirmed by EPR spin-trapping measurements. Few seconds of photoirradiation of the  $WO_3$  suspension in the presence of pbn causes the prompt formation of a triplet of doublets characterized by coupling constants  $aN = 15.4$  G,  $aH = 2.7$  G, which is shown in Figure S12. The coupling constant values are in agreement with the trapping of  $\cdot OH$  by pbn to form the paramagnetic adduct [pbn-OH]. These results confirm that photoexcited  $WO_3$  is able to initiate water oxidation by producing OH radicals. First, we can observe that the  $WO_3/st$ -type electrode reproducibly yields (max. relative standard deviation ca. 10%) much better results with respect to the state of the art [35] from which we adapted our preparative procedure, with an average limiting photocurrent of ca.  $2.2$  mA/cm<sup>2</sup>. This corresponds to a ca. 60% improvement over the reported case.  $WO_3/st$  is also a better performer compared to one of our best standard  $WO_3/coll$  (synthesis and characterization was previously published) [21] by a factor of ca. 40% (Figure S11). Interestingly, the  $WO_3/st$  J/V curve is generally steeper compared to the standards, suggesting low charge transport resistance across the oriented electrode and good interfacial charge separation efficiency. The global resistance  $R = (dV/dJ)$  figure of merit, comprising both the interfacial and the charge transport resistance, is indeed lower by a factor of 2 in the  $WO_3/st$  material (Nyquist Plots were compared in Figure S10). This confirms that the  $TiO_x$

adhesion layer offers a stable anchor for prolonged photoelectrode operation while being sufficiently permeable to electrons to allow for their efficient collection.

Current potential results were complemented by photon-to-electron conversion spectra: IPCE and APCE (Figure 6). IPCE% of  $\text{WO}_3/\text{st}$  and  $\text{WO}_3/\text{coll}$  are compared under 1 V and 1.5 V applied potential. We note that the limiting value of  $\text{WO}_3/\text{st}$  is reached with a reduced overpotential of ca. 0.5 V compared to  $\text{WO}_3/\text{coll}$ , consistent with the lower charge transfer resistance. First, we observe that IPCE is in good agreement with the J/V results, showing that the area subtended by the  $\text{WO}_3/\text{st}$  photoconversion is ca. 30% higher than that of  $\text{WO}_3/\text{coll}$ . It is also interesting to note that most of the improvement of  $\text{WO}_3/\text{st}$  comes from a better conversion in the visible region, from 400 to 500 nm. APCE% spectra confirm, for the  $\text{WO}_3/\text{st}$ , intrinsically higher charge transfer and charge transport efficiencies with respect to  $\text{WO}_3/\text{coll}$ . For the former, we record  $\text{APCE} \approx 70\%$  in the near UV, meaning that 70% of the photons absorbed in such a region is converted into useful charge carriers for driving an energetically demanding redox reaction. In the blue visible region, such efficiency is still significant, with a maximum value of the order of 50%. Consistent with the gap of ca. 2.7 eV, photoconversion ceases completely around 500 nm. The energy gap estimated from the photoaction spectra was confirmed by Tauc analysis (Supplementary Materials, Figure S13), displaying a reasonably linear region and affording an indirect band gap of 2.63 eV and a direct gap of 2.88 eV.

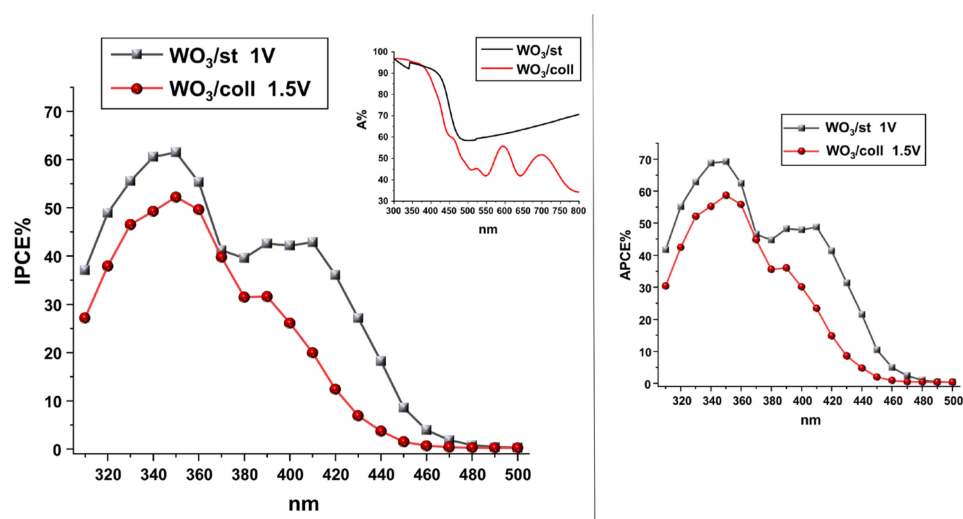


**Figure 6.** IPCE% and APCE% of  $\text{WO}_3/\text{st}$  and  $\text{WO}_3/\text{coll}$  under, respectively, 1 V and 1.5 V bias in 0.7 M  $\text{Na}_2\text{SO}_4$ . Their absorbance spectrum ( $A = 100 - R\% - T\%$ ) is shown in the inset.

We probed the impact of the presence of DRO, EE2 and OZ on the J/V characteristic of  $\text{WO}_3$  to gain direct indication of the photoelectrochemical degradation of these molecular targets. We note that the low solubility of DRO, EE2 and OZ in aqueous solution makes the direct observation of hole scavenging by these species impossible to be clearly observed by simply recording the photocurrent. For this reason, we explored the photoelectrochemical response of  $\text{WO}_3$  in  $\text{ACN}/0.1 \text{ M LiClO}_4$ , where concentrations of DRO, EE2 and OZ could be raised up to 0.01 M. The photocurrent recorded with blank  $\text{ACN}/\text{LiClO}_4$  solutions is due to both the oxidation of the residual water present in non-anhydrous  $\text{ACN}$  and the direct oxidation of the organic electrolyte [43].

In Figure S14, it is possible to observe, that, when DRO EE2 and OZ are present in the electrolyte, a 300 mV cathodic shift of the photoanodic onset potential occurs, associated with an increased photocurrent in the 0.2–0.8 V vs. SCE interval, a region of the J/V curve which is usually affected by electron/hole recombination losses. Both these effects are consistent with the fast capture of either holes or photogenerated radicals by the selected target organic species, resulting in their irreversible oxidation. We also point out that no

dark electrochemical processes resulting from the electrochemical oxidation of DRO, EE2 and OZ on the FTO/WO<sub>3</sub> surface are observed up to 1.8 V vs. SCE. We have thus provided direct evidence of the occurrence of the photoelectrochemical oxidation of DRO, EE2 and OZ at the illuminated WO<sub>3</sub> interface. Moreover, in the presence of DRO, EE2 and OZ, we generally observe a drop in the limiting photocurrent of the photoanodes, a fact that we have tentatively explained with the adsorption of the drug oxidation intermediates on the WO<sub>3</sub> surface, leading to a decreased active area of the photoelectrodes. In addition, EPR spin-trapping experiments were carried out on a WO<sub>3</sub> aqueous suspension containing DRO irradiated for few seconds in the presence of DMPO (see Section 2.3.4). It was observed the formation of the quartet (1:2:2:1, aN = aH = 14.8 G) was characteristic of the trapping of OH• radicals by DMPO (see Figure 7). After a few minutes, a triplet of doublets (aN = 15.36 G, aH = 20.28 G) appeared; these signals are possibly due to an adduct of a carbon radical originated from DRO and DMPO.

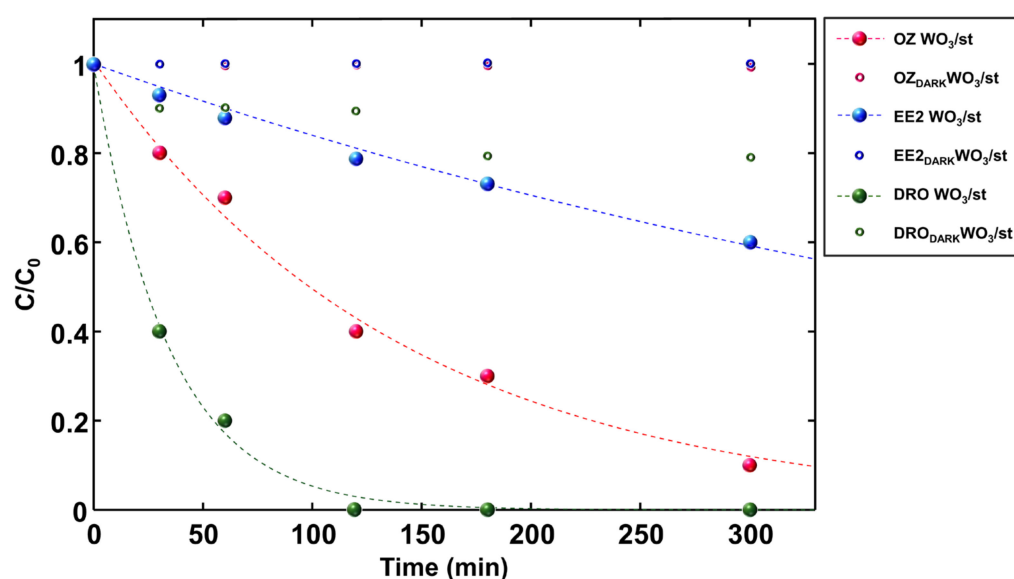


**Figure 7.** Photodegradation kinetics in batch system, data expressed as  $C/C_0$  vs. time; EE2 WO<sub>3</sub>/st, DRO WO<sub>3</sub>/st, OZ WO<sub>3</sub>/st represent the data of the irradiation experiments, EE2<sub>DARK</sub> WO<sub>3</sub>/st, DRO<sub>DARK</sub> WO<sub>3</sub>/st, OZ<sub>DARK</sub> WO<sub>3</sub>/st represent the data in dark conditions. Each solution was prepared at an initial concentration of 4 mg L<sup>-1</sup>.

### 3.3. Photochemical Degradation of DRO, EE2 and OZ

**Batch experiments.** To study the photocatalytic removal of the selected pharmaceuticals, batch experiments with and without the WO<sub>3</sub>/st photocatalyst, under irradiation and in dark conditions, were performed under the conditions described in Section 2.4. The concentration of the three tested drugs was determined by HPLC, as reported in Sections 2.4, 2.6 and 2.7. The determined concentration ( $C$ ) was divided by the initial concentration ( $C/C_0$ ). In the case of EE2 and OZ, in the absence of illumination, we demonstrated that the photocatalytic system does not contribute to drug adsorption. Indeed, the concentrations of neither EE2 nor OZ vary significantly under dark conditions, regardless of whether the catalyst is present or absent, and the ratio  $C/C_0$  is close to 1. A reduction of approximately 20% ( $C/C_0$  roughly 0.8) was observed only for the DRO molecule (as shown in Figure S15), and was thus likely attributable to an effective adsorption event. When comparing the results from the tests conducted in the darkness, it became evident that this specific pollutant is adsorbed onto the photocatalyst. Indeed, the data from dark conditions (in the absence of WO<sub>3</sub>/st) revealed no alterations in the DRO concentration, whereas a significant change was noted upon the addition of the photocatalyst (Figure S15). Moreover, the outcomes of irradiation tests conducted without the WO<sub>3</sub>/st powder indicate that the direct photochemical degradation of pollutants is in no case significant. On the

contrary, a remarkable decrease in the concentration of drugs was observed only when the test solution was irradiated in the presence of  $\text{WO}_3/\text{st}$ . Figure 7 shows the degradation kinetics of the three drugs, clearly indicating the occurrence of a photocatalytic process in the presence of the  $\text{WO}_3/\text{st}$  suspension.

Flow system experiments. For each pollutant (DRO, EE2 and OZ), the contribution to adsorption was investigated by evaluating the differences in the concentration determined by the HPLC of the contaminants in solution before and after contact with the glass spheres coated with  $\text{WO}_3/\text{st}$  ( $\text{WO}_3/\text{st-GS}$ ). In these experiments, 20 g of photoactive spheres were placed in a vial and kept in contact with 75 mL of aqueous solution for 420 min in the dark. The experimental data obtained showed that, for DRO, the uptake onto the  $\text{WO}_3/\text{st-GS}$  in (Figure S15) is negligible. Possibly, the difference in the adsorption of DRO onto the supported photocatalyst system  $\text{WO}_3/\text{st-GS}$  is even lower than that onto the  $\text{WO}_3/\text{st}$  due to the higher surface area of the latter one.

Experiments on the degradation kinetics by using the flow system (see Figure 3) were carried out by using 200 mL of 0.7 mM  $\text{Na}_2\text{SO}_4$  aqueous solution containing  $4 \text{ mg L}^{-1}$  of a drug to simulate the surface water conditions for what concerns both salinity and pH (see Section 2.4) [36]. Concerning the light absorption efficiency in the flow photoreactor, we have estimated, by exploiting diffuse reflectance measurements, that an attenuation of 400 nm light of ca. 60% (Figure S16) due to absorption by  $\text{WO}_3$  is achieved within an optical path of 1 cm. This is a similar attenuation to that observed with the  $\text{WO}_3/\text{st}$  suspension in static experiments (Figure S17). Considering that the diameter of the photoreactor is 2.2 cm, we obtain, along the radial coordinate, a nearly complete absorption (ca. 96%) of 400 nm light within the active volume of the reactor. In Figure 8, the results obtained using the flow system under irradiation are shown. Overall, a substantial drop in the concentrations of all pharmaceutical targets is observed upon the treatment of the test solutions in the flow reactor. However, the DRO and OZ degradation rates were smaller than those found in batch experiments. Possibly, the slower kinetics are due to the shorter contact time between the solution and the  $\text{WO}_3/\text{st}$  photocatalyst in the flow system with respect to the batch experiments. It has already been reported that, in a flow reactor, the immobilization of  $\text{WO}_3$  on a substrate leads to a lower activity [44]. Experimental data were fitted using a pseudo-first order (PFO) (1) kinetic equation. In the literature, many cases of pseudo-first order photocatalytic decomposition of organic compounds at similar concentrations in a flow reactor are reported [45,46]. In Table 2, the results obtained from both batch and flow experiments are shown.

From the data in Table 2, it can be seen that a  $\text{WO}_3$ -based photocatalyst is able to degrade all the selected drugs. Indeed, a  $\text{WO}_3$ -based photocatalyst, much like other semiconductor catalysts, is not selective, since the degradation reaction occurs through reactions with hydroxyl radicals ( $\text{OH}\bullet$ ), which are a strong oxidant characterized by an oxidation potential equal to  $E^\circ = +2.1 \text{ V vs. NHE}$ . In the case of EE2, the kinetic constants estimated from the flow and batch experimental data are higher than those of DRO and OZ. This could be explained by the presence, in the EE2 structure, of reactive OH groups and electron-rich carbon atoms. These functional groups likely serve as primary sites for initial reactions in the advanced oxidation process, potentially necessitating a shorter residence time within the flow reactor compared to DRO and OZ. Simultaneously, the flow configuration enhances the mass transfer of the drug within the reactor through convection, thereby increasing the likelihood of collisions between EE2 and the freely diffusing reactive oxygen species generated by the photocatalyst. Consistent with findings from batch experiments, DRO exhibits the highest degradation rate constant, leading to near-complete depletion from the test solution within 450 min. In the flow system, a  $\text{WO}_3$ -based photocatalyst operates under 400 nm irradiation, a condition under which it has already been proved that  $\text{WO}_3$  exhibits higher degradation efficiency of organic compounds with respect to other largely employed photocatalysts such as  $\text{TiO}_2$  [47]. The comparison of the results obtained in this study with the literature data is complicated due to the presence of numerous factors that can influence reactor performance [48]. Among

these factors, the type of photocatalyst is particularly significant. Photocatalytic activity is influenced not only by chemical composition but also by structural characteristics, dimensions, surface impurities, and the surface area. Only a few studies have been carried out to investigate the efficiency of  $\text{WO}_3$  in the photodegradation of the contaminants of emerging concern in a continuous flow reactor. Among them, Martins [44] had reported a transformation rate constant of  $3.5 \times 10^{-2} \text{ min}^{-1}$  and  $2.2 \times 10^{-2} \text{ min}^{-1}$  for tetracycline, obtained from two photoreactors having different configurations, which are of the same order of magnitude as those obtained in the present study.

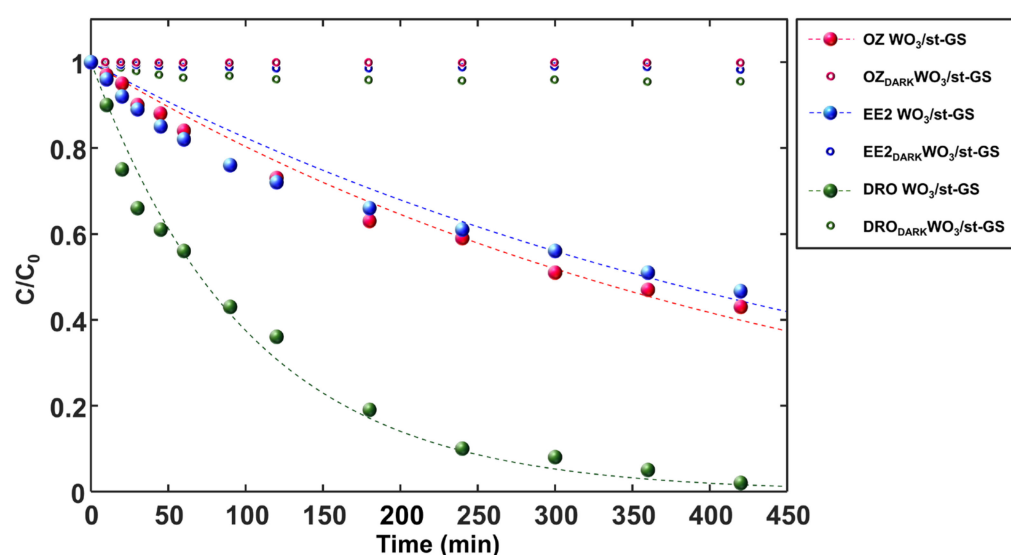


**Figure 8.** Drug photodegradation kinetics in the flow reactor, data expressed as  $C/C_0$  vs. time; EE2  $\text{WO}_3/\text{st}$ , DRO  $\text{WO}_3/\text{st}$ , OZ  $\text{WO}_3/\text{st}$  represent the data of the irradiation experiments, EE2<sub>DARK</sub>  $\text{WO}_3/\text{st}$ , DRO<sub>DARK</sub>  $\text{WO}_3/\text{st}$ , OZ<sub>DARK</sub>  $\text{WO}_3/\text{st}$  represent the data in dark conditions. Each solution was prepared at an initial concentration of  $4 \text{ mg L}^{-1}$ .

**Table 2.** Parameters obtained by non-linear fitting using a first-order kinetic model. The error is given as confidence interval at 95% of probability.

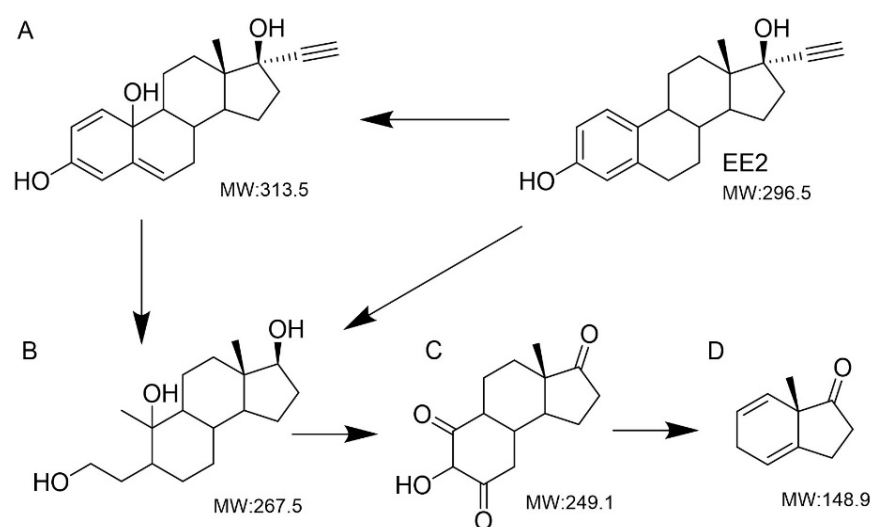
		$k_{\text{PFO}} (\text{min}^{-1})$	$R^2$
Batch	EE2 $\text{WO}_3/\text{st}$	$0.0018 \pm 0.0002$	0.9778
	DRO $\text{WO}_3/\text{st}$	$0.0293 \pm 0.0040$	0.9969
	OZ $\text{WO}_3/\text{st}$	$0.0071 \pm 0.0010$	0.9936
Flow	EE2 $\text{WO}_3/\text{st-GS}$	$0.0019 \pm 0.0002$	0.9313
	DRO $\text{WO}_3/\text{st-GS}$	$0.0098 \pm 0.0009$	0.9880
	OZ $\text{WO}_3/\text{st-GS}$	$0.0022 \pm 0.0002$	0.9694

### 3.4. Characterization of the Degradation Intermediates

After 8 h of circulation in the flow system, the EE2, DRO and OZ samples were analyzed by LC/MS in positive (DRO and OZ) and negative (EE2) ion modes. MS/MS data were acquired in order to establish the best ion transitions for use in MRM analysis. The instrument settings were adjusted to maximize the response of each precursor-product combination. Chromatographic separation of the compounds was achieved on a concentration gradient reversed-phase column with a total run time of 15 min at a flow rate of  $150 \mu\text{L}/\text{min}$ . The chromatograms of the different drugs were acquired by monitoring the  $m/z$  transitions  $295 > 145$  and  $295 > 143$  for the  $[\text{EE2} - \text{H}]^-$  ion. The  $[\text{DRO} + \text{H}]^+$  ion was monitored via the  $m/z$  transitions  $367 > 97$  and  $367 > 91$  and the  $[\text{OZ} + \text{H}]^+$  ion via the  $m/z$  transitions  $287 > 269$  and  $287 > 51$ . As mentioned earlier, the degradation of pharmaceuticals follows a scheme involving the reaction of contaminants with hydroxyl radicals

(OH•), whose presence has been confirmed through EPR measurements. A general scheme is reported in Supplementary Information (Scheme S1). In the following, the degradation intermediates originating from the oxidation of the three drugs investigated are described.

Mass spectrometry data show that EE2 was transformed into intermediate products of smaller molecular weight. To effectively track the conversion, it was necessary to identify the intermediates and by-products. The mass spectra show four characteristic peaks; the precursor ions detected in the sample were at  $m/z$  of 313, 267, 249, and 148. Compared with other studies on the photo-transformation products of EE2, it is found that the conversion of EE2 by HO• attack can occur, generating the by-products reported in Scheme 1 [49,50], according to a pathway consistent with the known reactivity of WO<sub>3</sub> upon band gap excitation in the presence of aqueous electrolytes. Reactive oxygen species like HO• are strong enough to break the C-C, C-O, and O-H bonds in the EE2 molecule and its intermediates. The overall photocatalytic degradation process of EE2 via WO<sub>3</sub>/st can be expressed as proposed in Scheme 1. HPLC/MS analysis confirms that, indeed, OH radicals are the main reactive oxidants in the photodegradation of EE2 in the presence of WO<sub>3</sub>/st due to the presence of hydroxylated intermediates. Intermediate A may correspond to a hydroxylated compound following the docking of OH with the addition of a hydroxyl group, linked to the benzene ring. Product B could be formed through processes such as oxidation, carbonyl, and ring breakdown. Product B, undergoing a sequence of oxidative attacks, could produce the oxygen-rich product C. The latter, after the complete oxidation and cleavage of the partly oxidized six-membered ring-bearing carbonyl and hydroxyl groups, affords the molecular ion D seen at  $m/z$  148 (see Table S1).

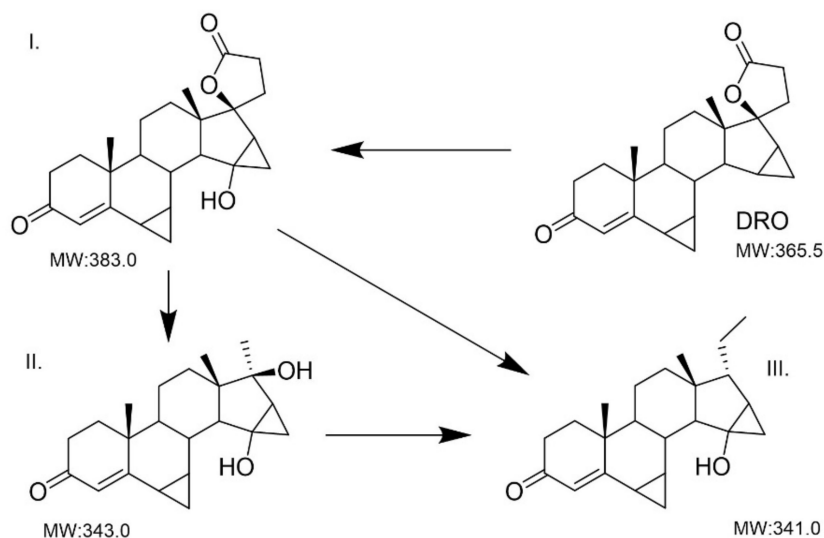


**Scheme 1.** Proposed EE2 degradation pathway and intermediates structures (A–D) according to LC/MS analysis.

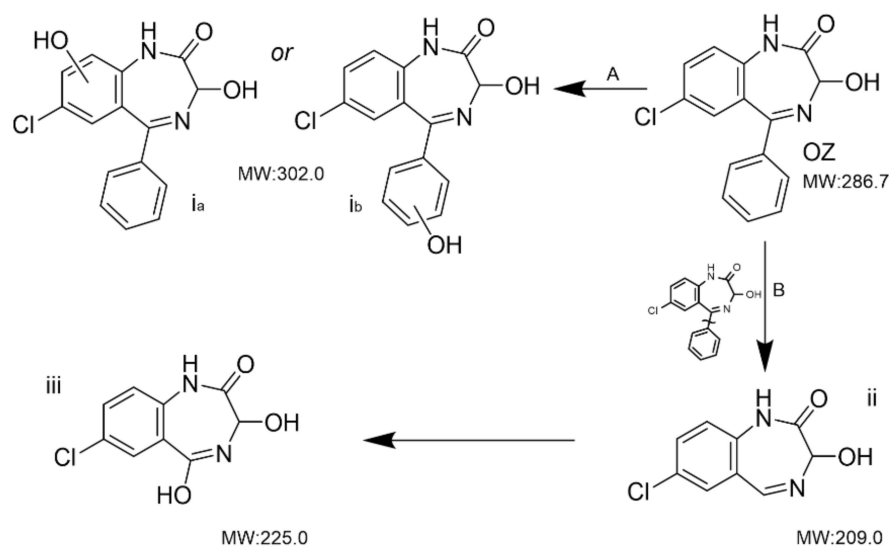
The photodegradation of DRO leads to the appearance of 383  $m/z$ , 343  $m/z$  and 341  $m/z$  peaks (see Scheme 2 and Table S2). The 383  $m/z$  by-product could be due to the addition of OH radicals onto the five-membered ring, similar to what was reported by Huang et al. [51] where the progesterone molecule (progenitor of the class to which DRO belongs) was studied. Subsequently, the oxidation process leads to the formation of other by-products, shorter than the starting molecules II and III.

HPLC/MS analyses were also carried out to study the photodegradation intermediates of the oxazepam molecule (see Table S3). Four by-products were identified which correspond to 302  $m/z$  (two possible structures), 225  $m/z$  and 209  $m/z$  peaks. The possible degradation pathway and photoproducted intermediates are shown in Scheme 3. As reported in other studies [52–54], where molecules such as alprazolam, which has similar structural characteristics as OZ and also belongs to the same benzodiazepine class, are inves-

tigated, it is hypothesized that the degradation of OZ may be mediated by photoproducted OH radicals as well.



**Scheme 2.** DRO degradation pathway and proposed intermediate structures (I–III) according to LC/MS analysis.



**Scheme 3.** Proposed OZ degradation pathways and proposed by-product structures (*ia*, *ib*–*iii*) according to LC/MS analysis.

From the HPLC/MS analysis, hydroxylated intermediates were, in fact, identified, indicating the attack of OH radicals (pathway A) on the aromatic ring to form the products *ia* and *ib*.

In pathway B, the oxazepam might undergo the cleavage of the bond between the nitrogen-containing heterocycle and the benzene ring, leading to detachment of the phenyl group (*ii*). Then, intermediate *ii* could be hydroxylated to product *iii* by further attack of OH radicals.

#### 4. Conclusions

This work has been focused on the application of oriented  $\text{WO}_3$  nanostructures with high photoelectrochemical activity to water remediation, exploiting advanced photocatalytic oxidation processes. Oxidative degradation of pharmaceuticals, selected among

steroid hormones and psychoactive drugs classified as high-priority emerging environmental contaminants, was successfully accomplished both in batch and flow photoreactors, with the latter exploiting easy-to-handle inert glass supports coated with solvothermally grown  $\text{WO}_3$  ( $\text{WO}_3/\text{st-GS}$ ). HPLC-MS analysis allowed for the separation and the clear identification of oxidation intermediates, pointing out that photogenerated HO radicals, generated upon the band gap excitation of  $\text{WO}_3$ , are the primary agents for the advanced oxidative degradation of all the selected pharmaceutical targets. The study of the degradation kinetics has shown a different rate of drug degradation in the batch reactor compared to the flow one. In two out of three cases, the batch system displayed faster kinetics, probably due to a more efficient contact between the solution and the photocatalyst. In fact, dispersing the catalyst in the form of a fine powder leads to a greater interfacial area, resulting in a more efficient production of OH radicals. Conversely, in the flow system,  $\text{WO}_3/\text{st}$  is immobilized on a solid support composed of millimeter-sized glass spheres, resulting in a decreased active surface/volume ratio and a less intimate contact with the solution carrying the drugs. This may result in the need for a longer treatment, particularly with robust molecules characterized by high chemical stability, like the family of benzodiazepines. Nevertheless, supported  $\text{WO}_3$  opens to easy handling and recovery of the photocatalyst and to the possibility of engineering flow systems suitable to treat larger volumes of contaminated water in a continuous fashion and with low counterpressure, while keeping the photocatalyst confined on a solid matrix.

**Supplementary Materials:** The following supporting information can be downloaded at: <https://www.mdpi.com/article/10.3390/nano14100860/s1>, Figure S1: Cyclic voltammetry of FTO, FTO- $\text{TiO}_x$  and FTO- $\text{TiO}_x$ - $\text{WO}_3$  seed layer in 0.01 M  $\text{K}_4\text{FeCN}_6$  and 0.1 M  $\text{LiClO}_4$ ; Figure S2: SEM image of  $\text{WO}_3/\text{coll}$ ; Figure S3: (a) Solar Simulator equipped with a AM1.5G filter and 380 nm UV cut-off filter, (b) 4  $\mu\text{g}/\text{mL}$  drug solution in vial under magnetic stirring; Figure S4:  $\text{WO}_3$  films solvothermally grown on FTO before (a) and after (b) the annealing process. Electrodes equipped with the  $\text{TiO}_x$  adhesion layer are indicated by (Ti) (i.e.,  $\text{WO}_3/\text{st-Ti-FTO}$ ); Figure S5: SEM image of  $\text{WO}_3/\text{st}$ ; Figure S6: EDS spectra of  $\text{WO}_3/\text{st}$ ; Figure S7: Phase identification for  $\text{WO}_3$  specimens grown on a microscope slide surface. The powder of both samples is mainly composed of  $\text{WO}_3$  in its monoclinic form ( $\text{P}2_1/\text{n}$ ; green reflections).  $\text{WO}_3$  in the hexagonal form ( $\text{P}6_3/\text{mcm}$ ; purple reflections) is also detected as associated minor phase; Figure S8: Rietveld refinement plots of the powder diffraction pattern for the  $\text{WO}_3/\text{st}$  specimens' growth on the microscope slide surface. The experimental profile is represented by black dots and the best-fit refinement profile is the flow red line. The lower green curve is the weighted difference between observed and calculated patterns. Vertical ticks mark the position of reflections for the identified phases in the two specimens. Figure S9: Glass column filled with  $\text{WO}_3/\text{st-GS}$ ; Figure S10: Nyquist plots of  $\text{WO}_3/\text{coll}$  (red) and  $\text{WO}_3/\text{st}$  (black) photoelectrode recorded at 0.6 V vs. SCE in 0.7 M  $\text{Na}_2\text{SO}_4$  under AM1.5G illumination. 10 mV sinusoidal perturbation in the range 20000-0.1 Hz; Figure S11: Average JV performance of a batch of  $\text{WO}_3/\text{st}$  photoanodes (black line) compared to some of our best internal standards  $\text{WO}_3/\text{coll}$  (green line). 0.7 M  $\text{Na}_2\text{SO}_4$  under AM1.5G illumination; Figure S12: EPR spectrum obtained after few seconds photoirradiation ( $\lambda > 400$  nm) of aqueous suspension of  $\text{WO}_3$  containing  $\text{H}_2\text{SO}_4$  (0.1 M) and pbn ( $5 \times 10^{-2}$  M); Figure S13: Tauc Plots of  $\text{WO}_3/\text{st}$  according to the direct (A) and indirect (B) transitions; Figure S14: J/V chopped curves under AM 1.5G illumination of  $\text{WO}_3$  in 0.1 M of  $\text{LiClO}_4$  in ACN solution in presence of 0.1 M of DRO (A) 0.1 M of EE2 (B) and 0.1 M of OZ; Figure S15: Comparison test (in presence of  $\text{WO}_3$ ): DRO in dark (DRODARK  $\text{WO}_3/\text{st}$ ), DRO irradiated (DRO  $\text{WO}_3/\text{st}$ ) and DRO in dark in batch system with spheres coated with  $\text{WO}_3$  (DRODARK  $\text{WO}_3/\text{st-GS}$ ); Figure S16: Transmission spectrum of  $\text{WO}_3/\text{st}$  loaded on glass spheres ( $[\text{T}\% (\text{WO}_3/\text{st-GS} - \text{T}\% \text{GS})]$ ) obtained with an integrating sphere in diffuse reflection mode along an optical path of 1 cm; Figure S17: Transmission spectra (1 cm optical path) of naked glass spheres GS,  $\text{WO}_3$  coated glass spheres ( $\text{WO}_3/\text{st-GS}$ ) and  $\text{WO}_3/\text{st}$  suspension (3.5 mg/mL) obtained in diffuse reflection mode; Scheme S1: Scheme for degradation of pollutants by  $\text{WO}_3$ ; Table S1: EE2 degradation intermediates, retention times, fragment ions and proposed structures; Table S2: DRO degradation intermediates, retention times, fragment ions and proposed structures; Table S3: DRO degradation intermediates, retention times, fragment ions and proposed structures.

**Author Contributions:** Methodology, formal analysis, investigation, writing—original draft, M.C., V.C. and C.S.; investigation, writing—original draft, M.A.; methodology, investigation, M.O.; data curation, T.C.; funding acquisition, supervision, writing—review and editing, A.M.; conceptualization, funding acquisition, supervision, writing—review and editing, S.C. and L.P. All authors have read and agreed to the published version of the manuscript.

**Funding:** The contribution at this work of M.C. was supported by the program PON “Research and Innovation” 2014–2020 (PON R&I), Action IV.6 “Contratti di ricerca su tematiche Green”. L.P., C.S., A.M. and S.C. acknowledge financial support from PNRR MUR project ECS\_00000033\_ECOSISTER. V.C. acknowledges PON Research and Innovation 2014–2020 (art. 24, comma 3, lett. (a), Law n. 240, 30 December 2010 and s.m.i. and D.M. n. 1062, 10 August 2021).

**Data Availability Statement:** Data are contained within the article.

**Acknowledgments:** The authors would like to acknowledge Negar Eftekhari and Cinzia Brenna of the Electron Microscopy Center of the University of Ferrara for additional SEM and EDS characterization.

**Conflicts of Interest:** The authors declare no conflicts of interest.

## References

1. Richardson, S.D.; Kimura, S.Y. Water Analysis: Emerging Contaminants and Current Issues. *Anal. Chem.* **2016**, *88*, 546–582. [[CrossRef](#)]
2. Vasilachi, I.C.; Asiminicesei, D.M.; Fertu, D.I.; Gavrilesco, M. Occurrence and fate of emerging pollutants in water environment and options for their removal. *Water* **2021**, *13*, 181. [[CrossRef](#)]
3. Mezzelani, M.; Gorbi, S.; Regoli, F. Pharmaceuticals in the aquatic environments: Evidence of emerged threat and future challenges for marine organisms. *Mar. Environ. Res.* **2018**, *140*, 41–60. [[CrossRef](#)] [[PubMed](#)]
4. Lazzara, R.; Blázquez, M.; Porte, C.; Barata, C. Low environmental levels of fluoxetine induce spawning and changes in endogenous estradiol levels in the zebra mussel *Dreissena polymorpha*. *Aquat. Toxicol.* **2012**, *106*, 123–130. [[CrossRef](#)] [[PubMed](#)]
5. Kelly, S.; Davies, E.; Fearn, S.; McKinnon, C.; Carter, R.; Gerlinger, C.; Smithers, A. Effects of oral contraceptives containing ethinylestradiol with either drospirenone or levonorgestrel on various parameters associated with well-being in healthy women: A randomized, single-blind, parallel-group, multicentre study. *Clin. Drug Investig.* **2010**, *30*, 325–336. [[CrossRef](#)] [[PubMed](#)]
6. Zhao, H.N.; Tian, Z.; Kim, K.E.; Wang, R.; Lam, K.; Kolodziej, E.P. Biotransformation of Current-Use Progestin Dienogest and Drospirenone in Laboratory-Scale Activated Sludge Systems Forms High-Yield Products with Altered Endocrine Activity. *Environ. Sci. Technol.* **2021**, *55*, 13869–13880. [[CrossRef](#)] [[PubMed](#)]
7. Zhao, Y.; Castiglioni, S.; Fent, K. Environmental Progestins Progesterone and Drospirenone Alter the Circadian Rhythm Network in Zebrafish (*Danio rerio*). *Environ. Sci. Technol.* **2015**, *49*, 10155–10164. [[CrossRef](#)] [[PubMed](#)]
8. Tang, Z.; Liu, Z.H.; Wang, H.; Dang, Z.; Liu, Y. A review of 17 $\alpha$ -ethynylestradiol (EE2) in surface water across 32 countries: Sources, concentrations, and potential estrogenic effects. *J. Environ. Manag.* **2021**, *292*, 112804. [[CrossRef](#)] [[PubMed](#)]
9. Yuan, S.F.; Liu, Z.H.; Lian, H.X.; Yang, C.T.; Lin, Q.; Yin, H.; Lin, Z.; Dang, Z. Fast trace determination of nine odorant and estrogenic chloro- and bromo-phenolic compounds in real water samples through automated solid-phase extraction coupled with liquid chromatography tandem mass spectrometry. *Environ. Sci. Pollut. Res.* **2018**, *25*, 3813–3822. [[CrossRef](#)]
10. Rocha, M.J.; Rocha, E. Synthetic Progestins in Waste and Surface Waters: Concentrations, Impacts and Ecological Risk. *Toxics* **2022**, *10*, 163. [[CrossRef](#)]
11. Avar, P.; Maasz, G.; Takács, P.; Lovas, S.; Zrinyi, Z.; Svigruha, R.; Takátsy, A.; Tóth, L.G.; Pirger, Z. HPLC-MS MS analysis of steroid hormones in environmental water samples. *Drug Test. Anal.* **2015**, *8*, 123–127. [[CrossRef](#)] [[PubMed](#)]
12. Fick, J.; Brodin, T.; Heynen, M.; Klaminder, J.; Jonsson, M.; Grabicova, K.; Randak, T.; Grabic, R.; Kodes, V.; Slobodnik, J.; et al. Screening of benzodiazepines in thirty European rivers. *Chemosphere* **2017**, *176*, 324–332. [[CrossRef](#)] [[PubMed](#)]
13. Vossen, L.E.; Červený, D.; Sarma, O.S.; Thörnqvist, P.O.; Jutfelt, F.; Fick, J.; Brodin, T.; Winberg, S. Low concentrations of the benzodiazepine drug oxazepam induce anxiolytic effects in wild-caught but not in laboratory zebrafish. *Sci. Total Environ.* **2020**, *703*, 134701. [[CrossRef](#)] [[PubMed](#)]
14. Salimi, M.; Esrafil, A.; Gholami, M.; Jafari, A.J.; Kalantary, R.R.; Farzadkia, M.; Kermani, M.; Sobhi, H.R. Contaminants of emerging concern: A review of new approach in AOP technologies. *Environ. Monit. Assess.* **2017**, *189*, 1–22. [[CrossRef](#)] [[PubMed](#)]
15. Sumpter, P.; Margiotta-Casaluci, L. Environmental Occurrence and Predicted Pharmacological Risk to Freshwater Fish of over 200 Neuroactive Pharmaceuticals in Widespread Use. *Toxics* **2022**, *10*, 233. [[CrossRef](#)] [[PubMed](#)]
16. Liu, Z.; Demeestere, K.; Hulle, S.V. Pretreatment of Secondary Effluents in View of Optimal Ozone-Based AOP Removal of Trace Organic Contaminants: Bench-Scale Comparison of Efficiency and Energy Consumption. *Ind. Eng. Chem. Res.* **2020**, *59*, 8112–8120. [[CrossRef](#)]
17. Cai, Q.Q.; Wu, M.Y.; Li, R.; Deng, S.H.; Lee, B.C.Y.; Ong, S.L.; Hu, J.Y. Potential of combined advanced oxidation—Biological process for cost-effective organic matters removal in reverse osmosis concentrate produced from industrial wastewater reclamation: Screening of AOP pre-treatment technologies. *J. Chem. Eng.* **2020**, *389*, 123419. [[CrossRef](#)]

18. Molinari, A.; Argazzi, R.; Maldotti, A. Photocatalysis with  $\text{Na}_4\text{W}_{10}\text{O}_{32}$  in water system: Formation and reactivity of OH radicals. *J. Mol. Catal. A Chem.* **2013**, *372*, 23–28. [[CrossRef](#)]
19. Luong, J.H.T.; Male, K.B.; Glennon, J.D. Boron-doped diamond electrode: Synthesis, characterization, functionalization and analytical applications. *Analyst* **2009**, *134*, 1965–1979. [[CrossRef](#)]
20. Yoshihara, S.; Muruganathan, M. Decomposition of various endocrine-disrupting chemicals at boron-doped diamond electrode. *Electrochim. Acta* **2009**, *54*, 2031–2038. [[CrossRef](#)]
21. Cristino, V.; Marinello, S.; Molinari, A.; Caramori, S.; Carli, S.; Boaretto, R.; Argazzi, R.; Meda, L.; Bignozzi, C.A. Some aspects of the charge transfer dynamics in nanostructured  $\text{WO}_3$  films. *J. Mater. Chem. A* **2016**, *4*, 2995–3006. [[CrossRef](#)]
22. Behbahani, M.A.; Ranjbar, M.; Kameli, P.; Salamati, H. Hydrogen sensing by wet-gasochromic coloring of  $\text{PdCl}_2(\text{aq})/\text{WO}_3$  and the role of hydrophilicity of tungsten oxide films. *Sens. Actuators B Chem.* **2013**, *188*, 127–136. [[CrossRef](#)]
23. Cristino, V.; Caramori, S.; Argazzi, R.; Meda, L.; Marra, G.L.; Bignozzi, C.A. Efficient photoelectrochemical water splitting by anodically grown  $\text{WO}_3$  electrodes. *Langmuir* **2011**, *27*, 7276–7284. [[CrossRef](#)] [[PubMed](#)]
24. De Tacconi, N.R.; Chenthamarakshan, C.R.; Yogeewaran, G.; Watcharenwong, A.; De Zoysa, R.S.; Basit, N.A.; Rajeshwar, K. Nanoporous  $\text{TiO}_2$  and  $\text{WO}_3$  films by anodization of titanium and tungsten substrates: Influence of process variables on morphology and photoelectrochemical response. *J. Phys. Chem. B* **2006**, *110*, 25347–25355. [[CrossRef](#)]
25. Watcharenwong, A.; Chanmanee, W.; de Tacconi, N.R.; Chenthamarakshan, C.R.; Kajitvichyanukul, P.; Rajeshwar, K. Anodic growth of nanoporous  $\text{WO}_3$  films: Morphology, photoelectrochemical response and photocatalytic activity for methylene blue and hexavalent chrome conversion. *J. Electroanal. Chem.* **2008**, *612*, 112–120. [[CrossRef](#)]
26. Hahn, R.; Macak, J.M.; Schmuki, P. Rapid anodic growth of  $\text{TiO}_2$  and  $\text{WO}_3$  nanotubes in fluoride free electrolytes. *Electrochem. Commun.* **2007**, *9*, 947–952. [[CrossRef](#)]
27. Daniel, M.F.; Lassegues, J.C.; Garie, R. Infrared and Raman Spectroscopies of rf Sputtered Tungsten Oxide Films. *J. Solid State Chem.* **1988**, *73*, 127–139. [[CrossRef](#)]
28. Leftheriotis, G.; Papaefthimiou, S.; Yianoulis, P. The effect of water on the electrochromic properties of  $\text{WO}_3$  films prepared by vacuum and chemical methods. *Sol. Energy Mater Sol. Cells* **2004**, *83*, 115–124. [[CrossRef](#)]
29. Meda, L.; Tozzola, G.; Tacca, A.; Marra, G.; Caramori, S.; Cristino, V.; Bignozzi, C.A. Photo-electrochemical properties of nanostructured  $\text{WO}_3$  prepared with different organic dispersing agents. *Sol. Energy Mater Sol. Cells* **2010**, *94*, 788–796. [[CrossRef](#)]
30. Santato, C.; Ulmann, M.; Augustynski, J. Photoelectrochemical properties of nanostructured tungsten trioxide films. *J. Phys. Chem. B* **2001**, *105*, 936–940. [[CrossRef](#)]
31. Santato, C.; Odziemkowski, M.; Ulmann, M.; Augustynski, J. Crystallographically oriented mesoporous  $\text{WO}_3$  films: Synthesis, characterization, and applications. *J. Am. Chem. Soc.* **2001**, *123*, 10639–10649. [[CrossRef](#)] [[PubMed](#)]
32. Park, J.H.; Bard, A.J. Photoelectrochemical tandem cell with bipolar dye-sensitized electrodes for vectorial electron transfer for water splitting. *Electrochem. Solid-State Lett.* **2006**, *9*, E5. [[CrossRef](#)]
33. Zhang, J.; Zhang, P.; Wang, T.; Gong, J. Monoclinic  $\text{WO}_3$  nanomultilayers with preferentially exposed (002) facets for photoelectrochemical water splitting. *Nano Energy* **2015**, *11*, 189–195. [[CrossRef](#)]
34. Wang, S.; Chen, H.; Gao, G.; Butburee, T.; Lyu, M.; Thaweesak, S.; Yun, J.H.; Du, A.; Liu, G.; Wang, L. Synergistic crystal facet engineering and structural control of  $\text{WO}_3$  films exhibiting unprecedented photoelectrochemical performance. *Nano Energy* **2016**, *24*, 94–102. [[CrossRef](#)]
35. Su, J.; Feng, X.; Sloppy, J.D.; Guo, L.; Grimes, C.A. Vertically aligned  $\text{WO}_3$  nanowire arrays grown directly on transparent conducting oxide coated glass: Synthesis and photoelectrochemical properties. *Nano Lett.* **2011**, *11*, 203–208. [[CrossRef](#)] [[PubMed](#)]
36. Cristino, V.; Pasti, L.; Marchetti, N.; Berardi, S.; Bignozzi, C.A.; Molinari, A.; Passabi, F.; Caramori, S.; Amidani, L.; Orlandi, M.; et al. Photoelectrocatalytic degradation of emerging contaminants at  $\text{WO}_3/\text{BiVO}_4$  photoanodes in aqueous solution. *Photochem. Photobiol. Sci.* **2019**, *18*, 2150–2163. [[CrossRef](#)] [[PubMed](#)]
37. Longobucco, G.; Pasti, L.; Molinari, A.; Marchetti, N.; Caramori, S.; Cristino, V.; Boaretto, R.; Bignozzi, C.A. Photoelectrochemical mineralization of emerging contaminants at porous  $\text{WO}_3$  interfaces. *Appl. Catal. B* **2017**, *204*, 273–282. [[CrossRef](#)]
38. Yang, H.G.; Sun, C.H.; Qiao, S.Z.; Zou, J.; Liu, G.; Smith, S.C.; Cheng, H.M.; Lu, G.Q. Anatase  $\text{TiO}_2$  single crystals with a large percentage of reactive facets. *Nature* **2008**, *453*, 638–641. [[CrossRef](#)] [[PubMed](#)]
39. Zhao, X.; Jin, W.; Cai, J.; Ye, J.; Li, Z.; Ma, Y.; Xie, J.; Qi, L. Shape- and size-controlled synthesis of uniform anatase  $\text{TiO}_2$  nanocuboids enclosed by active {100} and {001} facets. *Adv. Funct. Mater.* **2011**, *21*, 3554–3563. [[CrossRef](#)]
40. Zhang, D.; Wang, S.; Zhu, J.; Li, H.; Lu, Y.  $\text{WO}_3$  nanocrystals with tunable percentage of (001)-facet exposure. *Appl. Catal. B* **2012**, *123*, 398–404. [[CrossRef](#)]
41. Peng, T.; Ke, D.; Xiao, J.; Wang, L.; Hu, J.; Zan, L. Hexagonal phase  $\text{WO}_3$  nanorods: Hydrothermal preparation, formation mechanism and its photocatalytic  $\text{O}_2$  production under visible-light irradiation. *J. Solid State Chem.* **2012**, *194*, 250–256. [[CrossRef](#)]
42. Hu, Z.; Ji, Z.; Lim, W.W.; Mukherjee, B.; Zhou, C.; Tok, E.S.; Sow, C.H. K-Enriched  $\text{WO}_3$  nanobundles: High electrical conductivity and photocurrent with controlled polarity. *ACS Appl. Mater. Interfaces* **2013**, *5*, 4731–4738. [[CrossRef](#)] [[PubMed](#)]
43. Mi, Q.; Coridan, R.H.; Brunshwig, B.S.; Gray, H.B.; Lewis, N.S. Photoelectrochemical oxidation of anions by  $\text{WO}_3$  in aqueous and nonaqueous electrolytes. *Energy Environ. Sci.* **2013**, *6*, 2646–2653. [[CrossRef](#)]
44. Martins, A.S.; Guaraldo, T.T.; Wenk, J.; Mattia, D.; Zannoni, M.V.B. Nanoporous  $\text{WO}_3$  grown on a 3D tungsten mesh by electrochemical anodization for enhanced photoelectrocatalytic degradation of tetracycline in a continuous flow reactor. *J. Electroanal. Chem.* **2022**, *920*, 116617. [[CrossRef](#)]

45. Bhattacharjee, S.; Chakraborty, S.; Mandol, K.; Liu, L.; Choi, H.; Bhattacharjee, C. Optimization of process parameters during photocatalytic degradation of phenol in UV annular reactor. *Desalin. Water Treat.* **2015**, *54*, 2270–2279. [[CrossRef](#)]
46. Zheng, Q.; Aiello, A.; Choi, Y.S.; Tarr, K.; Shen, H.; Durkin, D.P.; Shuai, D. 3D printed photoreactor with immobilized graphitic carbon nitride: A sustainable platform for solar water purification. *J. Hazard. Mater.* **2020**, *399*, 123097. [[CrossRef](#)] [[PubMed](#)]
47. Mioduska, J.; Łapiński, M.S.; Karczewski, J.; Hupka, J.; Zielińska-Jurek, A. New LED photoreactor with modulated UV–vis light source for efficient degradation of toluene over WO<sub>3</sub>/TiO<sub>2</sub> photocatalyst. *Chem. Eng. Res. Des.* **2022**, *193*, 145–157. [[CrossRef](#)]
48. Binjhade, R.; Mondal, R.; Mondal, S. Continuous photocatalytic reactor: Critical review on the design and performance. *J. Environ. Chem. Eng.* **2022**, *10*, 107746. [[CrossRef](#)]
49. Mazellier, P.; Méité, L.; De Laat, J. Photodegradation of the steroid hormones 17β-estradiol (E2) and 17α-ethinylestradiol (EE2) in dilute aqueous solution. *Chemosphere* **2008**, *73*, 1216–1223. [[CrossRef](#)]
50. He, H.; Lin, Y.; Yang, X.; Zhu, X.; Xie, W.; Lai, C.; Yang, S.; Zhang, Z.; Huang, B.; Pan, X. The photodegradation of 17 alpha-ethinylestradiol in water containing iron and dissolved organic matter. *Sci. Total Environ.* **2022**, *814*, 152516. [[CrossRef](#)]
51. Huang, Z.; Lin, Q.; Luo, H.; Guo, P.; Weng, Q.; Lei, Y.; Cheng, S.; Liu, S.S. Degradation of progesterone by coexisting free radical and nonradical pathways in the CuO/HNTs-PS system. *J. Chem. Eng.* **2020**, *398*, 125458. [[CrossRef](#)]
52. Mitsika, E.E.; Christophoridis, C.; Kouinoglou, N.; Lazaridis, N.; Zacharis, C.K.; Fytianos, K. Optimized Photo-Fenton degradation of psychoactive pharmaceuticals alprazolam and diazepam using a chemometric approach—Structure and toxicity of transformation products. *J. Hazard Mater.* **2021**, *403*, 123819. [[CrossRef](#)] [[PubMed](#)]
53. Calisto, V.; Domingues, M.R.M.; Esteves, V.I. Photodegradation of psychiatric pharmaceuticals in aquatic environments—Kinetics and photodegradation products. *Water Res.* **2011**, *45*, 6097–6106. [[CrossRef](#)] [[PubMed](#)]
54. You, W.D.; Ye, P.; Yang, B.; Luo, X.; Fang, J.; Mai, Z.T.; Sun, J.L. Degradation of 17 Benzodiazepines by the UV/H<sub>2</sub>O<sub>2</sub> Treatment. *Front. Environ. Sci.* **2021**, *9*, 474. [[CrossRef](#)]

**Disclaimer/Publisher’s Note:** The statements, opinions and data contained in all publications are solely those of the individual author(s) and contributor(s) and not of MDPI and/or the editor(s). MDPI and/or the editor(s) disclaim responsibility for any injury to people or property resulting from any ideas, methods, instructions or products referred to in the content.